On the activity of comets: understanding the gas and dust emission from comet 67/Churyumov–Gerasimenko's south-pole region during perihelion

B. Gundlach,[1]⋆ M. Fulle [ID][2] and J. Blum[1]

[1]*Institut für Geophysik und extraterrestrische Physik, Technische Universität Braunschweig, Mendelssohnstr. 3, D-38106 Braunschweig, Germany*
[2]*Osservatorio Astronomico di Trieste, Instituto Nazionale Di Astrofisica, Via G. B. Tiepolo 11, I-34131 Trieste, Italy*

ABSTRACT

When comets approach the Sun, their surface is heated and the volatile species start to sublimate. Due to the increasing gas pressure, dust is ejected off the surface, which can be observed as cometary coma, dust tail, and trail. However, the underlying physical processes are not fully understood. Using state-of-the-art results for the transport of heat and gas as well as of the mechanical properties of cometary matter, we intend to describe the activity pattern of comets when they approach the Sun. We developed a novel thermophysical model to simulate the dust ejection from comet 67/Churyumov–Gerasimenko's south-pole region at perihelion. Based on the input parameters, this model computes the sub-surface temperature profile, the pressure build-up, and the redistribution of volatiles inside the cometary sub-surface region and provides mass-loss rates of dust and gas as well as typical sizes and ice content of the ejected dust chunks. Our thermophysical model allows for continuous gas and dust ejection from the Southern hemisphere of comet 67/Churyumov–Gerasimenko at perihelion. We find that the model output is in general agreement with the observed Rosetta data. The sublimation of CO_2 ice drives the ejection of very large ($\gtrsim 10\,cm$) chunks, which contain 10 per cent to 90 per cent of the initial water–ice content. In contrast, the outgassing of H_2O ice causes the lift-off of small clusters of dust aggregates, which contain no ice.

Key words: conduction – diffusion – methods: numerical – comets: general.

1 INTRODUCTION

Cometary nuclei are kilometre-sized objects, composed of different volatile and refractory species, i.e. ice and dust. They possibly formed in the protoplanetary disc by the gravitational collapse of pebble clouds, typically consisting of mm- to cm-sized aggregates of dust and ice (see e.g. Johansen et al. 2007; Blum et al. 2014, 2017; Lorek, Lacerda & Blum 2018), but alternative models exist in which pebbles play no role (Davidsson et al. 2016). After their formation, the cometary precursors were scattered into the outer regions of our Solar system, the Kuiper Belt and the Oort Cloud. Due to the large distance to the Sun, the bulk cometary material remained almost unaltered by solar radiation, and collisions among the cometary nuclei were unlikely or did not change their internal morphologies (Fulle & Blum 2017). Thus, comets are among the most primitive objects of our Solar system. When a cometary nucleus enters the inner Solar system after one or more gravitational-scattering events, the cometary surface warms up and the volatile components start to sublimate. Particles, aggregates, and chunks (see Fig. 1) are then ejected off the cometary surface into space. This process leads to the formation of the cometary coma, the dust tail, and the dust trail.

Several space missions studied the physical properties of comets (e.g. Deep Impact, Stardust, Rosetta, etc.), with the aim to understand cometary activity. Although these missions and particularly Rosetta have answered many questions about comets, the mystery of the general cometary activity has not been solved so far. One of the most important issues is how the low gas pressure that can build up by the sublimation of volatiles (Skorov & Blum 2012) can overcome the tensile strength of the near-surface material, which then allows lift-off of solids off the surface. Different solutions to increase the gas pressure (Fulle, Blum & Rotundi 2019), or to decrease the tensile strength, such as the existence of cracks (Skorov et al. 2016), the outgassing of super volatiles (Womack, Sarid & Wierzchos 2017), an ultralow tensile strength of the surface material (Blum et al. 2014; Attree et al. 2018), and the exothermic phase transition of amorphous to crystalline water ice (see e.g. Prialnik et al. 2008), were discussed in the past years.

All these effects require knowledge of the microphysical properties of the cometary surface to understand the details of the ejection process. Porosity, grain size-frequency distribution, hierarchical structures, composition; these microphysical properties can have a strong influence on the macrophysical properties of the surface
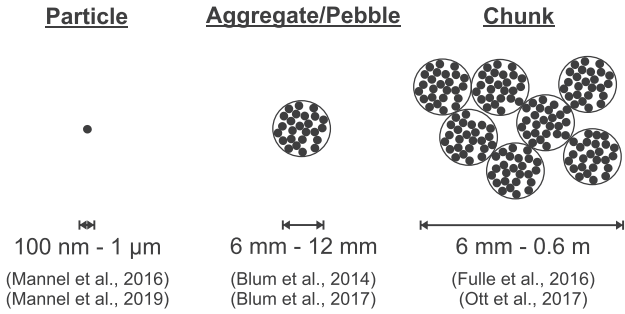
⋆ E-mail: b.gundlach@tu-bs.de

Figure 1. Particles are the smallest subunits of cometary matter, as measured by Mannel et al. (2016, 2019). During the formation process of planetary objects, dust aggregates (or pebbles) are formed from the particles (see Blum et al. 2014, 2017, for details). However, cometary activity can also lead to the ejection of large chunks made of aggregates (see Fulle et al. 2016; Ott et al. 2017, for details). For a review of dust morphologies observed with Rosetta, see Güttler et al. (2019).

layer, such as the tensile strength, the thermal conductivity, the heat capacity, and the gas permeability. These macrophysical properties determine the evolution of the temperature stratification and thereby the pressure build-up inside the cometary surface layers.

A valuable tool for a better understanding of how the microphysical properties influence the activity of comets is thermal modelling of the cometary subsurface layers. Many sophisticated models exist in the literature (see e.g. Hu et al. 2017; Keller et al. 2017; Prialnik & Sierks 2017). Our work is based on the paper on thermal modelling written by Davidsson & Skorov (2002) in which the authors discuss, besides many other important facets of modelling cometary activity, the modification of the heat transfer equation in order to take into account the latent heat of sublimation. We used this formulation in our work to develop a 1D thermophysical model, which solves the modified heat transfer equation for different depths below a cometary surface. As study case, we chose the south-polar region of comet 67P/Churyumov–Gerasimenko (hereafter 67P) during perihelion.

Our paper starts with reviewing the two different comet formation scenarios and their implications for the macrophysical properties of the cometary material (Section 2). In Section 3, a comprehensive overview of the different Rosetta observations, relevant for this work, is provided. Section 4 provides a general overview of the developed thermophysical model, with the details being presented in the respective Appendices. The results of our calculations are then presented and compared to the Rosetta measurements in Section 5. A discussion of our main findings and of the activity of comet 67P during perihelion is given in Section 6. Finally, the main results of this work are summarized in Section 7.

2 THE INTERNAL STRUCTURE OF COMETS

To understand the dust and gas activity of comets when they approach the Sun, knowledge of a number of physical processes is required. These questions comprise the absorption and transport of solar energy into the interior of the cometary nucleus as well as the efficiency of conversion of this energy into evaporating volatile species. Moreover, the tensile stresses need to be known to estimate from which sub-surface depths dust emission occurs. Before we present our thermophysical model of the cometary activity in Section 4, we will here estimate the determining physical quantities of the cometary matter, namely the thermal conductivity

as a function of temperature, the gas permeability, and the tensile strength, respectively. The thermal conductivity influences the temperature stratification of the sub-surface regions at any time, which, in turn, determines the evaporation/condensation rate of the volatiles at each depth; the gas permeability determines the transport of vapour into higher/lower depths, the local gas pressure, and the outgassing rate of the comet; finally, dust can be ejected if the local tensile strength is lower than the local pressure.

To determine these three quantities, knowledge about structure and mechanical properties is needed and these quantities depend on the formation and evolution of the cometary nucleus. Here, we follow the reviews by Blum (2018) and Weissman et al. (2019). The formation of planetesimals in the solar nebula started with the agglomeration of (sub-)micrometre-sized dust and ice particles into mm- to cm-sized aggregates, as described in detail by Zsom et al. (2010) and Lorek et al. (2018). These aggregates are called pebbles and have typical volume filling factors of 0.4, due to the domination of bouncing collisions (Zsom et al. 2010; Lorek et al. 2018). For the further evolution into planetesimals, two competing models have been presented: (i) further collisional growth (Windmark et al. 2012; Davidsson et al. 2016) and (ii) local concentration of the pebbles by hydrodynamic processes and subsequent gentle gravitational collapse (Youdin & Goodman 2005; Johansen et al. 2007; Blum et al. 2014, 2017). While model (i) predicts typical impact speeds of several $10\,\mathrm{m\,s^{-1}}$, which results in homogeneous, compacted dust layers, model (ii) predicts, due to the gentle nature of the gravitational collapse, that the pebbles survive the planetesimal formation intact so that a hierarchic structure results. Assuming that post-formation collisions do not substantially alter the internal structure of the planetesimals (Schwartz et al. 2018), the two formation models predict very different values for the thermal conductivity, the gas permeability, and the tensile strength, respectively.

(1) **Heat conductivity**: (i) The heat conductivity of a homogeneous dust layer resulting from the direct collisional sticking is only determined by the network thermal conductivity, decreases with increasing grain size (see Gundlach & Blum 2012a, for details) and is only weakly temperature dependent. Typical values are $10^{-1} - 10^{-3}\,\mathrm{W\,m^{-1}\,K^{-1}}$. Radiative heat transport can be neglected. (ii) The hierarchical pebble surface possesses a lower network heat conductivity, because of the highly reduced interparticle contacts between two neighbouring pebbles. Typical values range from $10^{-3} - 10^{-4}\,\mathrm{W\,m^{-1}\,K^{-1}}$. However, the radiative heat transport inside the voids between the pebbles can substantially increase the thermal conductivity to values of $10^{-1}\,\mathrm{W\,m^{-1}\,K^{-1}}$. This means that the thermal conductivity of pebble surfaces will be extremely low at low temperatures ($\lesssim 200\,\mathrm{K}$) and for small pebble sizes ($\lesssim 0.1\,\mathrm{mm}$), but can be very high for high temperatures ($\gtrsim 300\,\mathrm{K}$) and large pebbles ($\gtrsim 1\,\mathrm{mm}$).

(2) **Gas permeability**: the gas permeability determines how many molecules can escape into space from a sublimating ice surface through the covering dust layer (Gundlach, Skorov & Blum 2011). As the gas densities are in all cases extremely low, collisions among the molecules are unimportant with respect to collisions with the dust so that the gas permeability is determined by the mean free path between collisions with dust grains or pebbles and the number of dust or pebble layers. (i) Mean free paths in the collisional-sticking model are on the order of the grain size and, thus, typically ~ 1–$10\,\mu\mathrm{m}$ (for grain sizes of one micrometre and a volume filling factor of 0.2) and the number of dust layers per cm is several thousand. Therefore, the escape of gas from large depths

Table 1. H$_2$O and CO$_2$ outgassing rates, dust ejection rate, and size (distribution) of the ejected chunks from comet 67P at perihelion.

	Instrument	Mean rate	Range	References
H$_2$O Outgassing rate	MIRO	250 kg s^{-1}	150 – 430 kg s^{-1}	Marshall et al. (2017)
	ROSINA	640 kg s^{-1}	300 – 1000 kg s^{-1}	Hansen et al. (2016)
	SWAN	270 kg s^{-1}	–	Bertaux (2015)
CO$_2$ Outgassing rate	VIRTIS	50 kg s^{-1}	7 – 70 kg s^{-1}	Fougere et al. (2016)
	ROSINA	150 kg s^{-1}	35 – 350 kg s^{-1}	Fougere et al. (2016)
Dust ejection rate	OSIRIS	4400 kg s^{-1}	–	Ott et al. (2017)
Size of the chunks	OSIRIS	12.3 cm	5.7 – 26.6 cm	Ott et al. (2017)
Slope of the mass distribution function	OSIRIS	1/2	1/3 – 4/3	Ott et al. (2017)

is very difficult and the build-up of pressure is very efficient. (ii) In the case of gravitational collapse, the mean free path is of the order of several millimetres (for pebble sizes of one centimetre and a volume filling factor of the pebble packing of 0.5) and the number of layers per cm is close to unity. Thus, gas can efficiently escape and pressure build-up is only possible for dust thicknesses of several pebble layers.

(3) **Tensile strength**: (i) The tensile strength of the homogeneous dust layers resulting from the direct collisional sticking model has been measured in the laboratory for micrometre-sized silica and water–ice particles, is of the order of $\sigma_T \approx 1$ kPa and scales with the grain radius r as $\sigma_T \propto r^{-1}$ (Gundlach et al. 2018). (ii) A collection of mm- to cm-sized dust aggregates, as predicted by the gravitational collapse model, results in a much lower tensile strength of $\sigma_T \approx 0.1 - 1$ Pa and scales with the pebble radius R as $\sigma_T \propto R^{-2/3}$ (Skorov & Blum 2012; Blum et al. 2014; Brisset et al. 2016).

3 ROSETTA OBSERVATIONS DURING PERIHELION

The instruments on board the Rosetta spacecraft performed extensive measurements of the outgassing and dust ejection rates of comet 67P before, during, and after perihelion.[1] In the following, the measured outgassing and the dust ejection rates of comet 67P around perihelion are reviewed and are summarized in Table 1.

3.1 H$_2$O outgassing rate

The outgassing rate of H$_2$O was derived through inverse modelling of the MIRO data by Marshall et al. (2017). In this work, mean H$_2$O outgassing rates of 150 kg s^{-1} for the week before perihelion and of 430 kg s^{-1} for approximately 34 d after perihelion were derived. Because most of the data around perihelion were in the range between 0.6×10^{28} and 1.0×10^{28} s^{-1} (Fig. 6 in Marshall et al. 2017), we infer a mean H$_2$O outgassing rate of 250 kg s^{-1} for comet 67P at perihelion based on the MIRO measurements.

Another determination of the H$_2$O outgassing rate was provided by the ROSINA instrument, which utilized *in-situ* measurements of the gas density (COPS) and composition (DFMS). Hansen et al. (2016) derived a maximum outgassing rate of 1000 kg s^{-1} for approximately 20 d after perihelion. A minimum value for the outgassing rate measured by the ROSINA instrument can be derived by taking the lowest rates measured, i.e. 10^{28} s^{-1} (see fig. 6 in

Hansen et al. 2016), which yields 300 kg s^{-1}. Altogether, Hansen et al. (2016) derived a mean H$_2$O outgassing rate of 640 kg s^{-1}.

For comparison, Bertaux (2015) utilized data from the SWAN[2] instrument on board the *SOHO* satellite to derive an outgassing rate of 270 kg s^{-1}, which fits relatively well the MIRO observations.

3.2 CO$_2$ outgassing rate

While the H$_2$O activity followed the solar illumination pattern, the maximum of the CO$_2$ activity was always observed in the southern regions of comet 67P (see figs 5 and 7 in Läuter et al. 2019).

The CO$_2$ outgassing rates were derived from the VIRTIS and the ROSINA data. Because VIRTIS is a spectrometer, spectral line modelling together with a coma model is required to derive the CO$_2$ outgassing rates. From fig. 11 in Fougere et al. (2016), we can estimate that the CO$_2$ outgassing rates range from 10^{26} to 10^{27} s^{-1}, with a most probable value of 8×10^{26} s^{-1}. A translation into a mass-loss rate yields 7 to 70 kg s^{-1} with a favourable value of 50 kg s^{-1}.

Referring to Fougere et al. (2016), we can also derive the CO$_2$ outgassing rates measured by the ROSINA instrument. Their fig. 12 provides the information that the CO$_2$ outgassing rates are approximately a factor of ten lower than the H$_2$O outgassing rates. Fig. 11 can also be used to estimate the outgassing rates at perihelion. In this case, the CO$_2$ outgassing rates ranged from 5×10^{26} to 5×10^{27} s^{-1}, with a most probably value of 2×10^{27} s^{-1}, which provides mass-loss rates of 35 to 350 kg s^{-1} and a favourable value of 150 kg s^{-1}.

3.3 Dust loss rate and size (distribution) of the ejected chunks

The dust loss rates can be inferred by directly measuring the particle trajectories from the images taken by the OSIRIS cameras. Ott et al. (2017) derived the dust ejection rate of comet 67P during perihelion for different mass bins of the ejecta. Fig. 10 in Ott et al. (2017) shows that most of the mass was lost due to the ejection of chunks with masses between 0.1 and 10 kg. If we assume that most of the mass was ejected in 1 kg chunks and that the chunks possessed the same mass density as the nucleus (532 kg m^{-3}, following Jorda et al. 2016), we can calculate a typical chunk size (by assuming a cubic shape) of 12.3 cm. Hence, most of the mass is lost due to the ejection of chunks ranging from 5.7 cm (corresponding to a mass of 0.1 kg) to 26.6 cm (corresponding to a mass of 10 kg) in size.

---

[1]Perihelion: 13th of 2015 August.

[2]The SWAN instrument was designed to observe Lyman alpha photons at a wavelength of 121.6 nm, which are back-scattered by the neutral hydrogen atoms present in the interplanetary medium.

We recalculated the total mass-loss rate provided by Ott et al. (2017), because the authors assumed a density of $1000 \, \mathrm{kg \, m^{-3}}$ for the cometary material. Instead, we prefer to use a density of $532 \, \mathrm{kg \, m^{-3}}$ (Jorda et al. 2016). By using this density and by integrating the dust ejection rates over all mass bins, we derive a total dust ejection rate of $4400 \, \mathrm{kg \, s^{-1}}$ of comet 67P at perihelion (see Table 1).

Following again Ott et al. (2017), we can derive a power-law mass-frequency distribution function. For masses smaller than the peak mass of $\sim 1 \, \mathrm{kg}$ (see above), the slope is given by $\Pi_{\mathrm{Rosetta}} \approx +1/2$.

4 THERMOPHYSICAL MODEL

The aim of this paper is to better understand the cometary dust ejection process. Therefore, we developed a novel thermophysical model whose output parameters are compared with Rosetta observations of comet 67P during perihelion (see Section 3). This comparison allows the determination of several surface properties, as discussed in Section 5. This section, however, is dedicated to present the concepts of our thermophysical model. First, the general setting and the numerical techniques are described. Then, the input and output parameters of the model are presented. The section ends with an introduction of the different scenarios for which simulation runs were performed. For a better readability of this paper, we refrain in this Section from showing the whole set of equations and refer the interested reader to Appendix A.

4.1 The setting

We assume that the cometary nucleus consists of three massive components (see Fig. 2): (1) non-volatile dust particles (black dots in Fig. 2), (2) H_2O–ice particles (blue dots), and (3) CO_2–ice particles (orange dots with black rims), respectively, with relative mass abundances of f_{Dust}, $f_{\mathrm{H_2O}}$, and $f_{\mathrm{CO_2}}$ and normalization $f_{\mathrm{Dust}} + f_{\mathrm{H_2O}} + f_{\mathrm{CO_2}} = 1$. For the morphology, we considered two different cases (see Section 2): (i) a homogeneous composition with dust and ice particles of radii r, or (ii) a body consisting of monodisperse pebbles with radii R. We will also use the dust-to-ice mass ratio $f_{\mathrm{Dust}}/f_{\mathrm{Ice}} = f_{\mathrm{Dust}}/(f_{\mathrm{H_2O}} + f_{\mathrm{CO_2}})$ and the CO_2 ice content $f_{\mathrm{CO_2}}/f_{\mathrm{H_2O}}$ (see Table 2). It should be noted that the comet nucleus is porous, which is reflected in the bulk mass density of $532 \, \mathrm{kg \, m^{-3}}$ (Jorda et al. 2016), a value much smaller than any of the dust and ice material densities. The hierarchical or homogeneous porous structure resulting from the two formation scenarios has a strong influence on the heat conductivity, gas permeability, and tensile strength, as already mentioned in Section 2.

In our simulations, comet 67P is located at perihelion (with a heliocentric distance of 1.24 AU). We chose to model the case of maximum diurnal illumination, i.e. at the south pole with a constant solar elevation above horizon of $52°$ (Sierks et al. 2015). Hence, the Sun's position with respect to the surface normal is $\vartheta = 38°$ (see Fig. 2). During a polar day at perihelion, the Sun's elevation does not change, and for an observer on the cometary surface the Sun would move in a circle with constant elevation in the 'sky'.

Furthermore, we assume that the entire south-pole hemisphere of comet 67P was active at perihelion. This assumption is based on fig. 11 in Keller et al. (2015, right-hand panel). The total area of the south-pole region is $10 \, \mathrm{km^2}$.
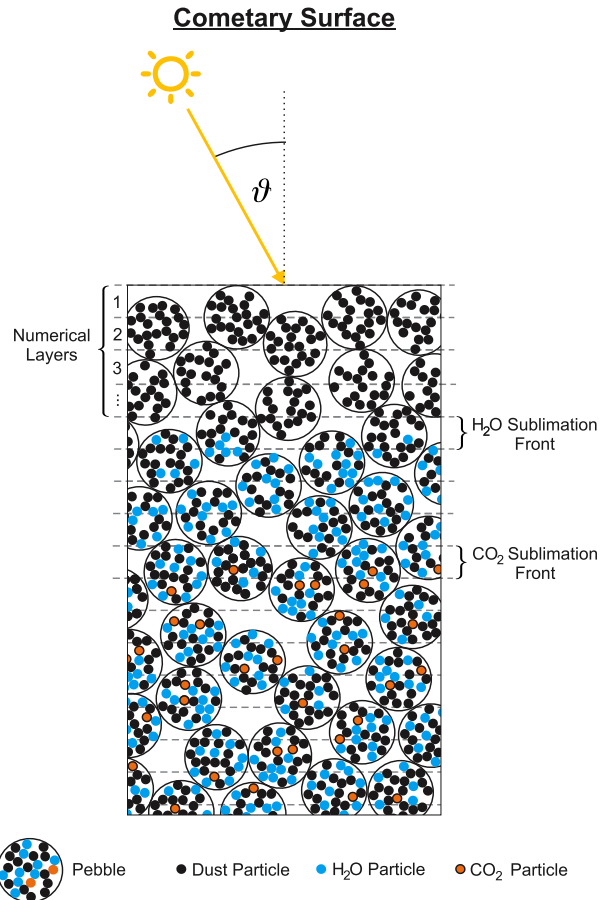

Cometary Surface

Figure 2. The setting used to model the dust activity of comet 67P at the south pole at perihelion. The Sun's zenith distance is $\vartheta = 38°$. The near-surface region of the comet nucleus consists of pebbles, which themselves are composed of non-volatile (siliceous and organic) dust, H_2O– and CO_2–ice particles. Due to the sublimation of the volatiles, the sublimation fronts move into the interior (downwards) with time if no dust emission occurs.

4.2 Numerical technique

The thermophysical model is based on different theoretical concepts and empirical findings. An overview of the concepts of the thermophysical model is provided in this Section and the details, such as the used equations and parameters, can be found in Appendix A.

For this work, we chose to model only a single isolated surface element of $1 \, \mathrm{m^2}$ cross-section, which means that we have not used a shape model of comet 67P. This strategy allowed us to spend the entire computational power to model the microphysical processes in the sub-surface layers in great detail and to study a wide range of different input parameters. In return, this parameter study provides the opportunity to derive the physical properties of the cometary subsurface by comparing the different model runs (scenarios) with Rosetta observations (see Section 5).

In order to model the microphysical processes in the sub-surface layers, we divided the cometary sub-surface into 512 layers. Each layer possesses a thickness, $\mathrm{d}x$, of one pebble radius, i.e. $\mathrm{d}x = R$ (see Fig. 2). Hence, the simulations cover depths of 1.3 to 6.4 m, for pebble radii from $R = 2.5 \, \mathrm{mm}$ to $R = 12.5 \, \mathrm{mm}$ (see Table 2). We also studied non-pebble cases (see Section 4.4 for details) for which we used a resolution of $\mathrm{d}x = 100 \, \mu\mathrm{m}$. The total dust

Table 2. Summary of the used input and output parameters.

	Input parameter			Output parameter	
	Parameter	**Symbol**	**Value**	**Parameter**	**Symbol**
	Dust-to-ice ratio	f_{Dust}/f_{Ice}	1, 2, 3, 4, 5, 6, 7, 8, 9, 10	H_2O outgassing rate	$\dot{\gamma}_{H_2O}$
	Pebble radius[1]	R	2.5, 5.0, 7.5, 10.0, 12.5 mm	CO_2 outgassing rate	$\dot{\gamma}_{CO_2}$
	CO_2 Ice content[2]	f_{CO_2}/f_{H_2O}	0.075, 0.15, 0.30, 0.45, 0.60 (constant σ_T)	Dust ejection rate	δ_{Dust}
	–	–	0.15–0.24 (variable σ_T)	Size of the Chunks[3]	x_{H_2O}, x_{CO_2}
	Permeability coefficient	b	1 or 7 Aggregate/Particle Diameter	Ice Content (Chunks)[4]	ξ_{H_2O}
	Thermal conductivity	λ	$\lambda_{Net} + \lambda_{Rad}$, 10^{-2} W m^{-1} K^{-1}, 10^{-3} W m^{-1} K^{-1}	–	–
or {	Constant tensile strength	σ_T	0.1, 0.2, 0.3, 0.4, 0.5, 0.6, 0.7, 0.8, 0.9, 1.0 Pa	–	–
	Depth-dependent strength	σ_0	1.0 Pa	–	–
	$\sigma_T(x) = \sigma_0 (1 + x/x_0)^{-1/2}$	x_0	1, 2, 3, 4, 5 cm	–	–

Notes. 1: Only used for the pebble case. For the variable tensile strength scenario, only $R = 5$ mm was used.
2: Relative to water ice content.
3: Dust ejection can be driven by the sublimation of H_2O or by the sublimation of CO_2.
4: Relative to initial H_2O–ice content. Only the large CO_2 driven chunks contain H_2O ice.

ejection and outgassing rates are then extrapolated by multiplying the derived rates for the single surface segment (with an area of 1 m^2, see Section 4.3) by the total area of the active south-polar region (10^7 m^2).

The core of the thermophysical model is the simultaneous treatment of the heat transfer equation (see Appendix A1.3) and the continuity equation for mass conservation (see Appendix A9) in each layer for each time-step. Technically, we applied the Crank–Nicolson method, which also provides the possibility to calculate inverse heat flows (inverted temperature profiles, e.g. at night; not used in this work). Based on the work of Davidsson & Skorov (2002), we modified the heat transfer equation and the mass conservation equation by adding a source/sink term, in order to take energy and pressure changes in each layer due to the sublimation/deposition process into account (see Appendix A for details about the sublimation and deposition process). Furthermore, the source/sink term also provides the option to model latent heat transport in the system. Therefore, the code counts the total number of ice molecules and the number of sublimated and deposited molecules in each layer. This task is performed for both ice species individually. This information is also used to monitor the ice content of the layers and of the ejected chunks.

For the treatment of the heat transfer equation, three different heat-transfer processes are considered, namely heat conduction through the solid particle contacts (network conduction), radiation between the pebbles (radiative transfer), and sublimation and deposition of molecules (latent heat transport; see Appendix A1.1 for a detailed description of these thermal transfer processes). As initial condition, the temperature array is set to 50 K at all depths. We assume that the solar input energy is only absorbed by the uppermost layer (see Appendix A5). The lower boundary condition is that the temperature is not allowed to heat the last numerical layer by more than 0.1 K.

Each numerical layer is given micro- and macrophysical properties. By setting these properties, the material type is chosen (continuous media approach). The used microphysical properties are grain and pebble radii, inneraggregate porosity, and ice contents (i.e. number of H_2O and CO_2 molecules per layer). From these microphysical properties, the macrophysical properties of the layers are derived, namely, the thermal conductivity (see equations A1–A7), the heat capacity (see equation A24), the sublimation and deposition rates (see equation A22), and the temperature (see

equation A23). Normally, the gas permeability[3] and the tensile strength[4] are also set by the material composition and grain/pebble size. However, we decided to keep these two parameters variable to investigate their influence on the results of the thermophysical model (see Section 4.3). Because we consider relatively high dust-to-ice ratios (see Section 4.3), the code uses a constant mass density for all layers ($\rho = 532$ kg m^{-3}), irrespective of the ice contents. The global volume filling factor (or the porosity) is chosen such that each layer possesses the above-mentioned mass density. Hence, $\phi_{agg} = 0.4$ is the volume factor inside the pebbles (i.e. 60 per cent void space inside the pebbles) and $\phi_{pack} = 0.6$ is the volume filling factor of the pebble packing (i.e. 40 per cent void space between the pebbles).
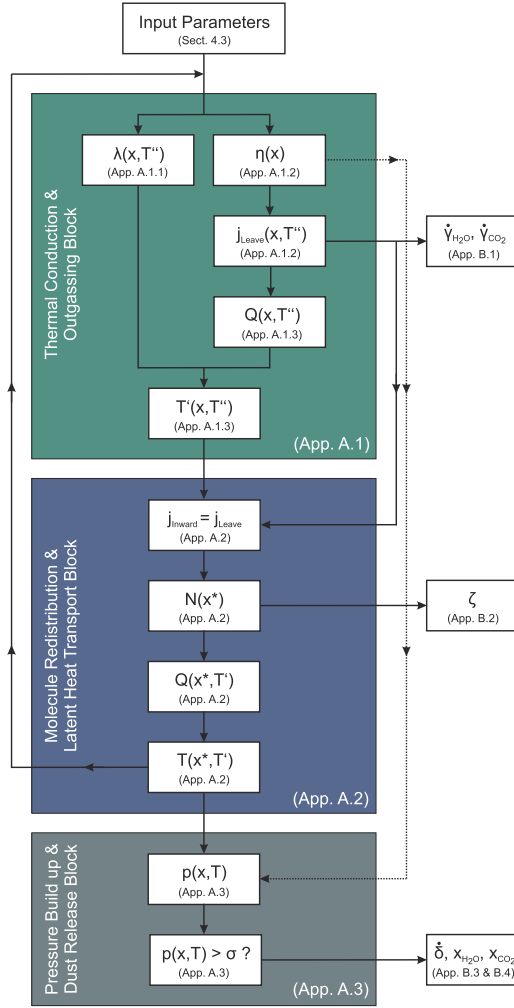
Based on the used input parameters (see Section 4.3), the code performs calculations in three blocks for each time-step, dt, and for each depth element, dx, starting with the uppermost layer. Fig. 3 provides a step-wise overview of the performed computations with links to the respective Appendices. The three different main blocks are described in the following.

The first block (see Appendix A1) utilizes the temperature profile derived in the prior time-step, $T''(x)$, to calculate the thermal conductivity, $\lambda(x, T'')$, and the sublimation rate, $j(x, T'')$. Therefore, the position x of the actual layer is important, because the number of overlying dust layers determines the efficiency of the outgassing rate, $\eta(x)$ (the number of sublimating molecules is not equal to the number of molecules able to escape into space). Based on the escape rate, the cooling rate is derived, which is then used together with the heat conductivity to compute the resulting temperature change of the considered layer. Hence, this block provides the intermediate temperature profile $T'(x, T'')$ and outgassing rates, $\dot{\gamma}_{H_2O}$ and $\dot{\gamma}_{CO_2}$, of the two ice species (see Appendix B for details).

The task of the second block (see Appendix A2) is the redistribution of the sublimated molecules into the interior, $j_{Inward}(x, T)$, and the calculation of the resulting transport of energy (latent heat). The active layer loses energy, $Q(x, T)$, according to the

---

[3]The gas permeability can be expressed by the diffusion constant, which linearly depends on the aggregate size (effective Knudsen diffusivity; see equation 13 in Gundlach et al. 2011).
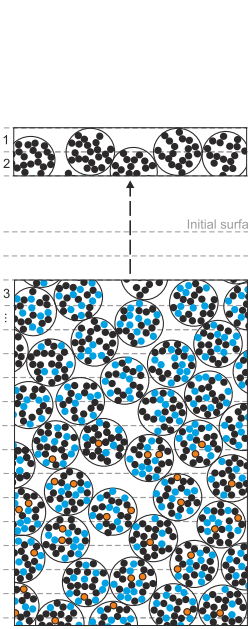[4]The tensile strength σ_T also depends on the pebble size, $\sigma_T \propto R^{-2/3}$ (Skorov & Blum 2012).

Figure 3. The concept of the thermophysical model visualized by a flow diagram. The used input parameters are discussed in Section 4.3 and Table 2. Readers interested in details of the thermophysical model are referred to the Appendices as shown in the flow diagram. The used model parameters are summarized in Table A1.
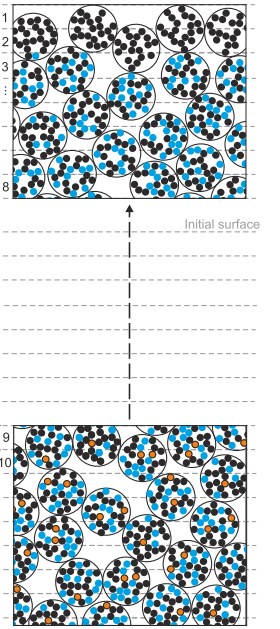

Figure 4. Graphical visualization of the ejection events. If the erosion condition is met (see equations A27 and A28), the overlying numerical layers are counted and removed from the simulation. The pressure build-up of H_2O gas (left-hand panel) ejects small, ice-free chunks, whereas the pressure build-up of CO_2 gas (right-hand panel) causes the ejection of larger, H_2O ice-containing chunks.

number of sublimated molecules, and this energy is deposited into deeper layers, $Q(x^*, T)$. Hence, this block also influences deeper layers (indicated by x^* in Fig. 3), by changing the number of ice molecules, $N(x^*)$ and the temperature of the underlying layers. This block provides an updated temperature profile $T(x, T')$, which also serves as input for the next time iteration. If an ejection event occurs, this block is also used to derive the ice content, ξ, of the emitted chunks. In order to calculate the number of inward diffusing molecules, we assume that the same number of molecules that are lost into space also diffuse inwards. Because of our earlier work (Gundlach et al. 2011), we know how many escaping molecules we can expect from a sublimating ice surface buried beneath a dust layer. If inward gas diffusion is allowed, the total number of sublimating molecules capable to leave the considered layer is, thus, twice the outgassing rate into space. It is important to

note that this is an ad-hoc assumption that we have tested in Section 6.1.6.

Finally, the third block (see Appendix A3) utilizes the updated temperature profile together with the efficiency of the outgassing rate $\eta(x)$ (indicated by the dotted line in Fig. 3) to derive the resulting pressure profile, $p(x, T)$. The pressure in each layer is compared with the assumed tensile strength of the material. If the pressure in the considered layer exceeds the tensile strength, all layers above are ejected. Numerically, the ejection event is treated by deleting the ejected layers and by shifting all respective arrays by the number of lost layers. New layers are added at the bottom. These new layers have an initial temperature of 50 K. With this method, the heat wave never reaches the bottom of the simulated slab if ejection repeats continuously. As output parameters, this third block provides the dust ejection rate, $\dot{\delta}_{Dust}$, as well as the size of the ejected chunks, x_{H_2O} and x_{CO_2}. Here, x_{H_2O} and x_{CO_2} stand for the H_2O and CO_2 driven ejection events.

Each simulation run is stopped when exactly fifty ejection events have occurred, or when the time threshold was reached. In principle, both volatile constituents are able to trigger ejection events (see Fig. 4). The pressure build-up of the CO_2 gas typically removes larger chunks (several numerical layers), which contain H_2O ice, whereas the H_2O gas pressure build-up causes the ejection of smaller, ice-free chunks. It is important to mention that the code does not calculate the dynamical evolution of the ejected chunks, it just removes the layers from the simulation and counts the number of layers that are lost.
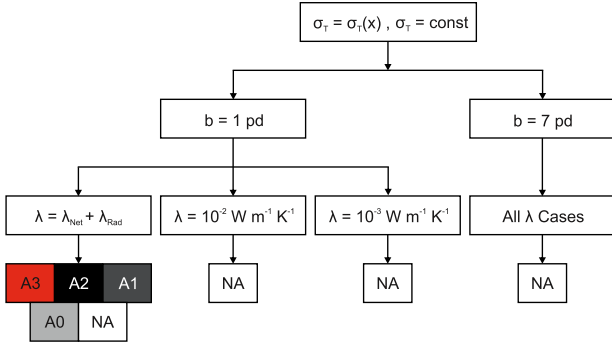
Figure 5. Overview of the different scenarios studied with our thermophysical model. In total, we studies twelve different scenarios, by varying the tensile-strength law (two cases; constant versus depth-dependent tensile strength), the gas permeability parameter (two cases; $b = 1$ pd versus $b = 7$ pd), and the thermal conductivity (three cases: $\lambda = \lambda_{\mathrm{Net}} + \lambda_{\mathrm{Rad}}$ versus $\lambda = 10^{-3}$ W m^{-1} K^{-1} versus $\lambda = 10^{-2}$ W m^{-1} K^{-1}), respectively. In only three of these twelve cases, dust activity (levels A0–A3; see Section 5 for details) could be measured; all other cases show no dust activity (NA).

We tested different time-step settings (details can be found in Appendix A4) and found that d$t = 100$ s provides a good compromise between numerical stability and time efficiency.

4.3 Input and output parameters

The thermophysical model depends on six different input parameters, i.e. the dust-to-ice ratio, $f_{\mathrm{Dust}}/f_{\mathrm{Ice}}$, the pebble radius, R, the CO_2–ice content, f_{CO_2}/f_{H_2O}, the permeability coefficient, b, the heat conductivity, λ, and the tensile strength, σ_{T} (see Table 2). The dust-to-ice ratio describes the mass ratio of the dust to the ice components (H_2O and CO_2 ice). The CO_2–ice content is defined relative to the H_2O–ice content. For example, a dust-to-ice ratio of 4 and a CO_2–ice content of 0.15 means that 80 per cent of the mass consists of dust, 17.4 per cent of H_2O ice, and 2.6 per cent of CO_2 ice. For almost all cases, we started with CO_2–ice contents of 0.075, 0.15, 0.30, 0.45, and 0.60. However, for the cases with depth-dependent tensile strength (see Section 4.4), we found that only runs with a CO_2–ice contents between 0.15 and 0.24 showed dust ejection. Hence, we decided to vary the CO_2–ice content in this interval with a finer step size of 0.01 in these cases.

The tensile strength is another input parameter and is set to constant values (see Table 2), or decreases with increasing chunk size (or depth; i.e. depth-dependent tensile strength). For the cases with chunk-size-dependent tensile strength, we decided to decrease computation time by only using one fixed pebble size of $R = 5$ mm. Although the homogeneous dust layer case intrinsically possesses a much higher tensile strength of $\sim$1 kPa (Gundlach et al. 2018), we also allowed for the very low tensile strengths that are typical for pebble surfaces.

In the pebble case, the thermal conductivity is determined by radiation and conduction ($\lambda_{\mathrm{Net}} + \lambda_{\mathrm{Rad}}$), whereas the radiation can be neglected in the homogeneous case, due to the small mean free path of the photons within the voids of the material. Hence, we assumed $\lambda = \mathrm{const} = 10^{-2}$ W m^{-1} K^{-1} and $\lambda = \mathrm{const} = 10^{-3}$ W m^{-1} K^{-1} for the homogeneous case. Latent heat transport is taken into account in all cases.

The thermophysical model provides six output parameters, i.e. the outgassing rates of the two volatile components, $\dot{\gamma}_{H_2O}$ and
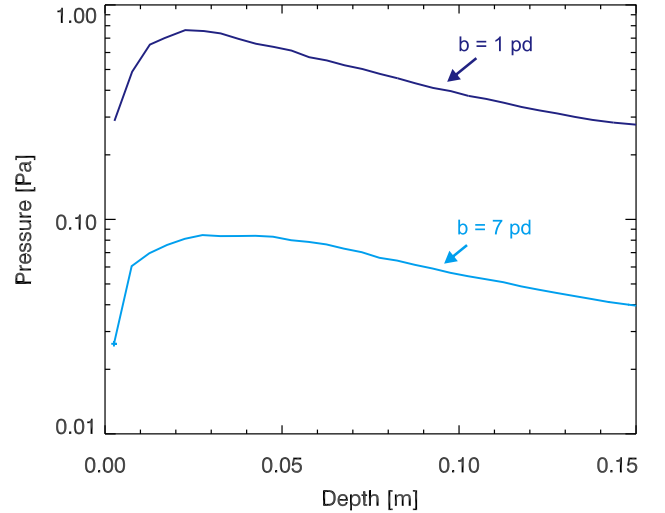

Figure 6. Pressure build-up in the cometary sub-surface layers caused by the sublimation of H_2O ice. The $b = 7$ pd case (Gundlach et al. 2011) yields lower pressures due to the relatively higher permeability of the material. The $b = 1$ pd case (Skorov et al. 2011) causes significant higher pressures (lower permeability of the material). The pressure profiles are extracted from the same run as shown in Fig. 7 ($\lambda = \lambda_{\mathrm{Net}} + \lambda_{\mathrm{Rad}}$ case). pd: particle/pebble diameter.

$\dot{\gamma}_{CO_2}$, measured in [kg s^{-1}], the total dust ejection rate, $\dot{\delta}_{\mathrm{Dust}}$, also measured in [kg s^{-1}], the mean size of the ejected chunks, x_{H_2O} and x_{CO_2}, given in [cm] and the H_2O–ice content of the ejected chunks, ξ_{H_2O} (measured relative to the initial H_2O–ice content). Please note that CO_2 ice was never observed in the ejected chunks. A detailed mathematical definition of the output parameters can be found in Appendix B.

4.4 Scenarios

In order to test several situations, we investigated 12 different scenarios as shown by Fig. 5. These scenarios are set by three different input options:

(i) **Tensile strength (σ_{T}):** We studied two cases for the tensile strength, i.e. (i) a size-independent strength $\sigma_{\mathrm{T}} = \mathrm{const} = 0.1 - 1$ Pa, and (ii) a depth-dependent strength $\sigma_T(x) = \sigma_0 (1 + x/x_0)^{-1/2}$, with a fixed $\sigma_0 = 1.0$ Pa and a variable $x_0 = 1 - 5$ cm (see Table 2). The latter behaviour is known from solid-state physics and means that materials become weaker the larger their spatial dimensions are, because the chance for failures increases with increasing size. Here we chose to also test this idea and follow the scaling described by Bažant (1999).

(ii) **Permeability coefficient (b):** The permeability coefficient is a measure of how thick a layer of dust is required to reduce the outgassing flux of a pure ice surface at a given temperature to 50 per cent of the value without dust cover (Gundlach et al. 2011). Hence, this parameter defines the efficiency of the outgassing rate $\eta(x)$ as discussed in Appendix A1.2. This parameter directly controls the rate of molecules lost into space and also determines the pressure build-up in the sub-surface layers. A higher value of b, for example $b = 7$ pd (pd: pebble, or particle diameter), results in a higher escape rate into space and in less pressure build-up in the sub-surface layers. In contrast, lower b values, e.g. $b = 1$ pd cause a higher pressure build-up for the same thickness of the dust cover, but fewer molecules are lost into space. Fig. 6 exemplifies

the maximum pressure (not to be confused with a pressure profile at one given time-step) in each layer for two simulation runs based on the same input parameters, but for different b values. Here, the $b = 1$ pd case provides higher pressures inside the sub-surface than the $b = 7$ pd case.

(iii) **Heat conductivity (λ):** We used different options for the heat conductivity corresponding to the two sub-surface morphologies, (i) $\lambda = \text{const} = 10^{-2}\,\text{W}\,\text{m}^{-1}\,\text{K}^{-1}$ and $\lambda = \text{const} = 10^{-3}\,\text{W}\,\text{m}^{-1}\,\text{K}^{-1}$ represent the homogeneous-dust-layer cases, in which radiation in the void space is negligible, because of the very short mean free path of the photons. (ii) A subsurface structure consisting of pebbles, as formed in the gravitational-collapse scenario (see Section 2), possesses a strong contribution by radiative transport, due to the large voids in the material so that we can write for the heat conductivity, $\lambda = \lambda_{\text{Net}} + \lambda_{\text{Rad}}$. The different thermal conductivity equations have a major influence on the resulting temperature profiles and, thus, on all derived output parameters as can be seen in Fig. 7. In all cases, latent heat transport is considered.

In principle, the tensile strength (see Skorov & Blum 2012, for details), the gas-permeability coefficient (see Gundlach et al. 2011, for details), and the heat conductivity (see Gundlach & Blum 2012b, for details) are fully determined by the used material structure and composition. However, to also allow alternative settings, we considered the scenarios discussed above (see Fig. 5).

5 RESULTS

We ran simulations as described in the previous Section with all combinations of the input parameters displayed in Table 2. In the case of depth-dependent tensile strength, the total number of runs was 500 per permeability coefficient b and thermal conductivity λ. For constant tensile strength, we ran 2500 simulations per permeability coefficient b and thermal conductivity λ (see Fig. 5). Recurrent dust activity and ejection of large chunks (> 6 cm) was observed only for the pebble model, i.e. for a temperature-dependent heat conductivity, and only for $b = 1$ pd (see Fig. 5). In the case of depth-dependent tensile strength, 224 runs out of the 500 simulation runs (45 per cent) yielded recurrent dust activity. For constant tensile strength, 676 out of 2500 simulations (27 per cent) resulted in dust activity. The no-pebble cases (constant thermal conductivity) have not shown recurrent dust activity, because α **(the surface-to-volume ratio)** in equation (A25) had to be computed by using the particle radius, $r = 1\,\mu\text{m}$, instead of the pebble radius, R (this parameter is not relevant in the no-pebble case). Consequently, the outgassing rate is much higher and, hence, the sublimation front can be found at greater depths. However, at greater depths, the temperature is lower and pressures of 0.1 to 1.0 Pa cannot be reached. Hence, no continuous dust eject was observed for the no-pebble case.

Fig. 8 shows an example of a run with repeated dust activity. The four time snapshots are taken (i) immediately before an H_2O-driven dust ejection, (ii) immediately after an H_2O-driven dust ejection, (iii) immediately before a CO_2-driven dust ejection, and (iv) immediately after a CO_2-driven dust ejection, respectively. As can be seen, our simulations allow us to distinguish between the two possible causes for dust ejection, namely when the H_2O-gas pressure or the CO_2-gas pressure exceeds the local tensile strength. In Fig. 8, it can be seen that the evolution of the cometary surface is very regular in time. Whenever the local gas pressure (plotted as pluses for H_2O and crosses for CO_2 in the lowermost panels) exceeds the tensile strength (in this case $\sigma_T = 0.5$ Pa, see the horizontal
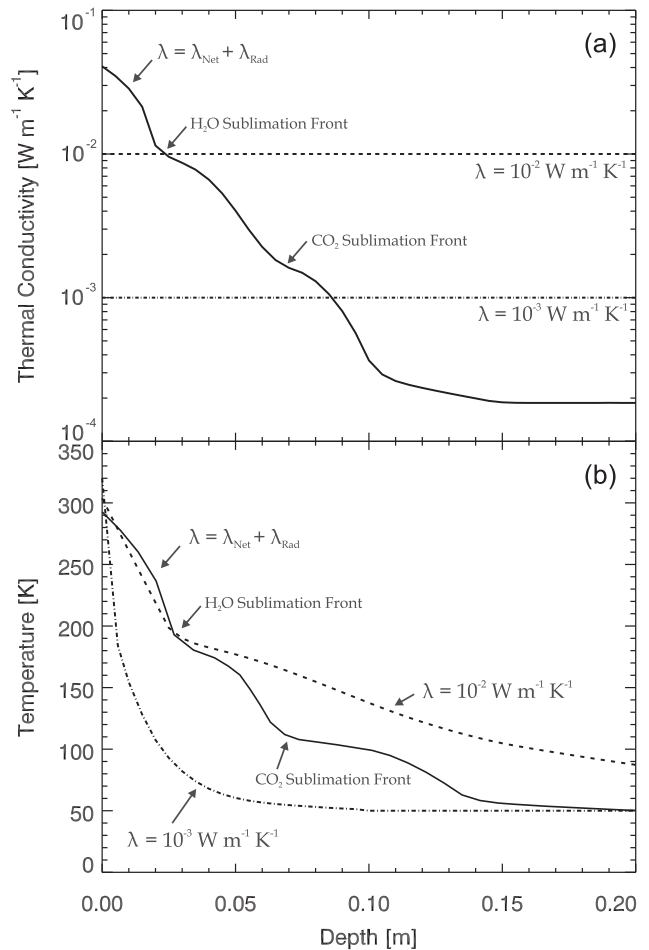

Figure 7. (a) The three heat-conductivity cases used in this study. The dashed and dash-dotted constant heat conductivities represent the homogeneous model, whereas the solid curve characterizes the pebble case in which the radiative heat transfer is important for high temperatures (i.e. for shallow depths) (b) The resulting temperature-depth curves. It should be noted that the dips in the temperature profile are caused by latent cooling due to sublimation. The profiles are extracted 26000 s after the start of the simulation. In the cases of $\lambda = \lambda_{\text{Net}} + \lambda_{\text{Rad}}$ and $\lambda = 10^{-2}\,\text{W}\,\text{m}^{-1}\,\text{K}^{-1}$, the H_2O sublimation front is located at 0.025 m depth, whereas the CO_2 sublimation front can be found in deeper layers (at 0.07 m). For comparison, in the low thermal conductivity case ($\lambda = 10^{-3}\,\text{W}\,\text{m}^{-1}\,\text{K}^{-1}$) less energy is transported into the interior so that the sublimation fronts are still located very close to the surface. It can also be seen that the lower thermal conductivity causes a higher surface temperature.

dash-dotted line in the lowermost panels) with two ejections of chunks with ~ 1.5 cm size, caused by H_2O sublimation, followed by one emission of a ~ 8 cm-sized chunk, caused by CO_2 evaporation (see vertical dotted and dashed lines for ejections caused by H_2O and CO_2, respectively). The topmost panels in Fig. 8 show the temperature as a function of depth (compare Fig. 7b), with the characteristic signatures for the evaporation fronts of H_2O and CO_2. The middle panels show with pluses and crosses, respectively, the contents of H_2O and CO_2 ice, normalized to the original values. A comparison between Figs 8(a) and (b) shows that the emitted dust chunks are completely desiccated, whereas the chunks ejected due to CO_2 activity still contain water ice (compare Figs 8c and d). The emitted mass rates for H_2O and CO_2 vapour as well as for dust are calculated by assuming that the simulations represent
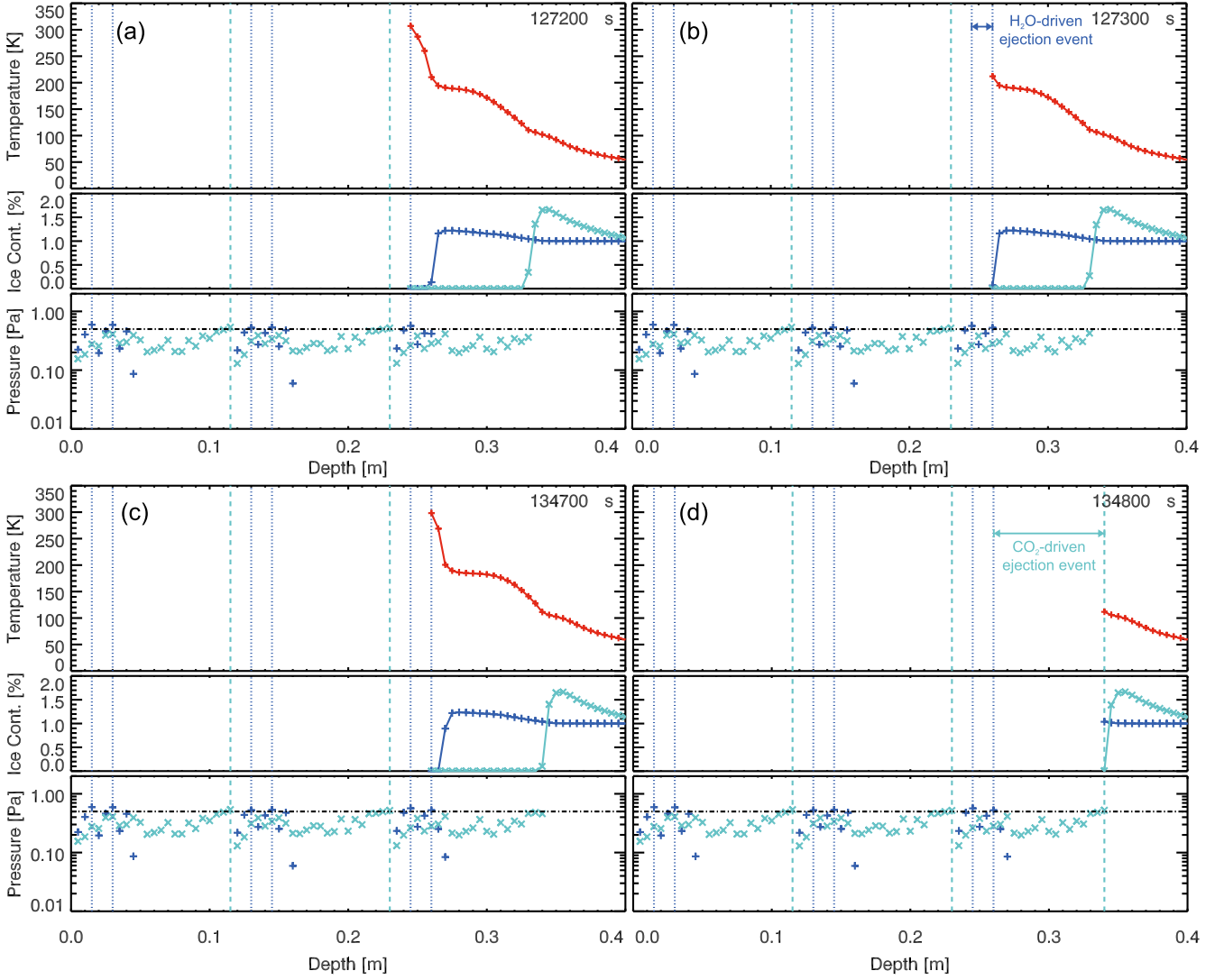
Figure 8. Example of a run with repeated dust activity. The four time snapshots are taken (a) immediately before a H_2O-driven dust ejection, (b) immediately after a H_2O-driven dust ejection, (c) immediately before a CO_2-driven dust ejection, and (d) immediately after a CO_2-driven dust ejection, respectively. Numbers indicated in the top right of each of the four panels refer to the elapsed time since start of the simulation. More details can be found in the text. The used input parameters are: $\sigma_T = 0.5\,\mathrm{Pa}$, $R = 5\,\mathrm{mm}$, $f_{Dust}/f_{Ice} = 3$, and $f_{CO_2}/f_{H_2O} = 0.3$. The first ten ejection events (visualized by the vertical dashed and dotted line) of this simulation run are also available as a movie: Fig 8 movie.wmv.

$1\,\mathrm{m}^2$ of area and that the whole layer is emitted simultaneously. For the mass of the individual ejected dust chunks, we assume that the ejected dust layer breaks up into identical chunks with cubic shape whose side lengths equal the thickness of the ejected layer.

5.1 Criteria for matching the Rosetta observations

Whenever dust activity was observed, we applied three primary criteria to assess whether the results match the Rosetta observations:

(i) **Criterion 1:** The first criterion demands that the simulated outgassing and dust ejection rates are individually not lower than and do not deviate relative to each other more than a factor of two

from the Rosetta values, i.e.

$$\dot{\gamma}_{H_2O,Sim} \geq \dot{\gamma}_{H_2O,Rosetta} \quad \text{and}$$

$$\dot{\gamma}_{CO_2,Sim} \geq \dot{\gamma}_{CO_2,Rosetta} \quad \text{and}$$

$$\dot{\delta}_{Dust,Sim} \geq \dot{\delta}_{Dust,Rosetta} \quad \text{and}$$

$$0.5 < \left(\frac{\dot{\gamma}_{CO_2,Sim}}{\dot{\gamma}_{CO_2,Rosetta}}\right) \Big/ \left(\frac{\dot{\gamma}_{H_2O,Sim}}{\dot{\gamma}_{H_2O,Rosetta}}\right) < 2 \quad \text{and}$$

$$0.5 < \left(\frac{\dot{\delta}_{Dust,Sim}}{\dot{\delta}_{Dust,Rosetta}}\right) \Big/ \left(\frac{\dot{\gamma}_{H_2O,Sim}}{\dot{\gamma}_{H_2O,Rosetta}}\right) < 2. \quad (1)$$

Here, the indices 'Sim' and 'Rosetta' denote the simulation results and the Rosetta data (see Section 3), respectively. With the normalization in equation (1), we make sure that the dust-to-gas and CO_2-to-H_2O outflow rates are consistent with Rosetta observations, without deciding about the actual mass-loss rates.

(ii) **Criterion 2:** The second criterion is used to search for all runs that result in mass-flux ratios between the large (i.e. CO_2-driven) and small (i.e. H_2O-driven) chunks compatible with Rosetta

observations. For the latter, we compare to the data published by Ott et al. ([2017](#)). For the definition of the slope parameter ($Q_{\text{Slope Ratio}}$), see Appendix B5. Hence, the second criterion reads

$$Q_{\text{Slope Ratio}} \geq 2/3. \tag{2}$$

This criterion ensures that only simulation runs that are consistent with the size distribution observed by Rosetta (Ott et al. [2017](#)) are taken into account. It is important to mention that our model together with this criterion can only explain the ejection of pebbles larger than the smallest size ($\sim 6\,\text{mm}$) found by Ott et al. ([2017](#)). The model cannot (or only extremely rarely) emit only chunks, but almost always shows emission of chunks and pebbles simultaneously. If every square metre on 67P would be identical, a bimodal size distribution of pebbles and chunks would result, which contradicts the findings by Rosetta. However, there might be variations of some, or all, parameters that we assumed in our simulations across the illuminated surface of 67P (illumination conditions, local shadowing, pebble sizes, tensile strength, dust-to-ice ratio, CO_2–ice content). Thus, at this stage, we assume that what Rosetta measures is a mixture of all those conditions. If we make sure (by adopting criterion 2) that any single simulation that we consider as a possible solution has the same slope as measured by Rosetta, then any combination of results also fulfills the slope criterion. Figs [10](#) and [11](#) show that there are potentially several simulations with comparable slope ratios but very different chunk sizes. So, in principle it is possible to retrieve the full-size distribution measured by Rosetta, but this needs much more elaborate simulations, which should be the aim of a future study. An explanation for the ejection of smaller particles will be provided in another upcoming paper (Fulle et al. [2020](#)).

(iii) **Criterion 3:** Finally, the size of the largest emitted chunks should be in the range found for comet 67P, i.e.

$$x_{\text{CO}_2} = 5.7 - 26.6\,\text{cm} \tag{3}$$

(see Section 3.3).

5.2 Categorization of the results

We categorized the results of the individual runs according to the following scheme:

(i) **No (dust) activity (NA):** the local gas pressure never reached or exceeded the local tensile strength so that the main criterion for dust activity was never met. It should be noted that these runs did show gas activity, though.

(ii) **Activity level 0 (A0):** although recurrent dust activity was observed, neither of the above three criteria were matched.

(iii) **Activity level 1 (A1):** exactly one of the above criteria was matched.

(iv) **Activity level 2 (A2):** two out of the three criteria were matched.

(v) **Activity level 3 (A3):** All three criteria were simultaneously matched.

5.3 Most important findings

In the following, we will describe the most important findings:

(i) For all activity levels, the ratio between the rates of ejected dust and emitted CO_2 vapour is approximately equal to the original dust-to-CO_2-ice ratio (see Fig. [9](#)). This is not the case for the dust-to-H_2O-vapour ratio and the dust-to-ice ratio, because dust can be emitted through either H_2O or CO_2 sublimation, where in the
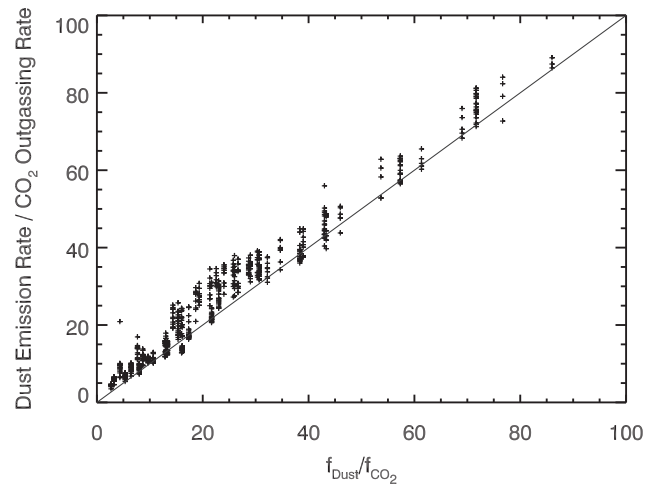

Figure 9. Dust-to-CO_2-vapour emission as a function of the original dust-to-CO_2-ice ratio inside a simulated comet nucleus with constant tensile strength (**all constant tensile strength simulations**). The diagonal line shows where input and output are identical, as expected for the emission of CO_2-ice-free dust chunks.

latter case the chunks are not desiccated. Thus, as long as there are sufficiently many CO_2-driven dust-ejection events, the dust-to-CO_2-vapour ratio is a good proxy for the dust-to-CO_2-ice ratio inside the nucleus.

(ii) A permeability parameter of $b = 7\,\text{pd}$ (pd: pebble, or particle diameter, see Section 4.4) always resulted in NA, due to the too low pressure build-up (see Fig. [6](#)).

(iii) None of the cases for the homogeneous comet nucleus (i.e. the cases without pebbles), in which we used a constant heat conductivity of $\lambda = 10^{-2}\,\text{W}\,\text{m}^{-1}\,\text{K}^{-1}$ or $\lambda = 10^{-3}\,\text{W}\,\text{m}^{-1}\,\text{K}^{-1}$, resulted in activity level A0, A1, A2, or A3. The explanation for this circumstance is given in Section 6.1.3.

(iv) For the pebble case, i.e. for a temperature-dependent heat conductivity, activity level A3 was reached for a few parameter combinations. Table [3](#) shows a complete list of the A3 cases.

5.4 Correlations between the output parameters

Figs [10](#) and [11](#) summarize the correlations between the outputs of all simulations with pebbles in the categories A0–A3 for the cases of size-dependent tensile strength (Fig. [10](#)) and constant tensile strength (Fig. [11](#)), respectively. In the case of size-dependent tensile strength, criterion 1 (see equation 1) was fulfilled for most of the runs as can be seen in the inset of Fig. [10](#). Thus, most of the simulations yielded the correct relations between the outgassing rates of H_2O and CO_2 and the dust ejection rate, although the individual values are typically a factor of ~ 2 above the measured rates. We will discuss this point further in Section 6.1. Criterion 2, the slope of the mass distribution function, is also fulfilled in many of the simulated cases, although the majority of slope ratios are significantly lower than unity and cluster around 0.8. However, the biggest restriction comes from criterion 3, i.e. the size of the chunks. As can be seen in Fig. [10](#), most of the simulations eject too small chunks (around 1 cm in size) so that only a few cases were observed to eject chunks with sizes around 10 cm. Future tests with $\sigma_0 > 1\,\text{Pa}$ will check if much larger chunks may be ejected in the depth-dependent tensile strength case.

Table 3. Summary of all A3 cases. The bold numbers represent the mean values of the input and output parameters.

				Variable tensile strength						
Input parameters					Output parameters					
Scale length	Radius	D:I	CO_2 Cont.	$\dot{\gamma}_{H_2O}$ / $\dot{\gamma}_{H_2O,R}$	$\dot{\gamma}_{CO_2}$ / $\dot{\gamma}_{CO_2,R}$	$\dot{\delta}_{Dust}$ / $\dot{\delta}_{Dust,R}$	$Q_{Slope\ Ratio}$	Size (x_{CO_2})	Ice Cont.	$\bar{\sigma}(x_{CO_2})^\dagger$
1 cm	5 mm	2	0.16	2.22	4.36	2.89	0.74	11.3 cm	0.87	0.3 Pa
2 cm	5 mm	2	0.15	1.96	2.77	1.89	0.85	6.4 cm	0.83	0.5 Pa
2 cm	5 mm	2	0.16	2.05	3.60	2.39	0.84	15.2 cm	0.85	0.3 Pa
3 cm	5 mm	10	0.21	1.35	0.91	1.77	1.60	14.4 cm	0.48	0.4 Pa
4 cm	5 mm	3	0.23	2.22	4.16	2.50	0.90	8.4 cm	0.79	0.6 Pa
4 cm	5 mm	7	0.21	1.75	1.44	2.00	1.35	7.9 cm	0.58	0.6 Pa
4 cm	5 mm	7	0.22	1.79	1.61	2.10	1.28	8.4 cm	0.60	0.6 Pa
4 cm	5 mm	7	0.23	1.85	1.77	2.24	1.21	9.0 cm	0.61	0.6 Pa
5 cm	5 mm	6	0.24	1.77	2.00	2.07	∞	15.9 cm	0.61	0.5 Pa
(3.2 ± 1.3) cm	–	**5.1 ± 2.9**	**0.20 ± 0.03**	**1.89 ± 0.27**	**2.51 ± 1.26**	**2.21 ± 0.34**	**1.12 ± 0.29***	**(10.8 ± 3.6) cm**	**0.69 ± 0.14**	**(0.49 ± 0.13) Pa**
				Fixed tensile strength						
Input parameters					Output parameters					
Tensile Str.	Radius	D:I	CO_2 Cont.	$\dot{\gamma}_{H_2O}$ / $\dot{\gamma}_{H_2O,R}$	$\dot{\gamma}_{CO_2}$ / $\dot{\gamma}_{CO_2,R}$	$\dot{\delta}_{Dust}$ / $\dot{\delta}_{Dust,R}$	$Q_{Slope\ Ratio}$	Size (x_{CO_2})	Ice Cont.	
0.4 Pa	12.5 mm	4	0.15	2.41	3.58	4.64	1.22	7.2 cm	0.59	–
0.5 Pa	12.5 mm	2	0.15	2.34	4.57	3.29	1.09	14.1 cm	0.56	–
0.4 Pa	10 mm	2	0.15	2.30	4.31	3.24	0.70	10.1 cm	0.47	–
0.7 Pa	12.5 mm	4	0.30	3.51	6.39	3.79	0.70	20.0 cm	0.58	–
(0.5 ± 0.1) Pa	–	**3.0 ± 1.2**	**0.19 ± 0.08**	**2.64 ± 0.58**	**4.71 ± 1.19**	**3.74 ± 0.65**	**0.93 ± 0.27***	**(13.0 ± 4.9) cm**	**0.55 ± 0.06**	–

Notes. Radius: radius of the dust aggregates; D:I: dust-to-ice ratio; R: Rosetta; Size: mean size of the large chunks; ∞: only CO_2-driven ejection events.
$\dagger$: $\bar{\sigma}(x_{CO_2})$ is the mean tensile strength at location of breakup.
*: the infinite value is ignored.

In the case of constant tensile strength, criterion 1 (emission/ejection rates) is only fulfilled for a small subset of runs (see inset of Fig. 11), with many cases lying outside the factor-of-two window that criterion 1 allows. Criterion 2 (slope ratio) is also fulfilled in part of the simulations, but many runs cluster around slope ratios of 0.5. In contrast to the size-dependent tensile strength, a constant tensile-strength value produces on average bigger chunks so that criterion 3 is fulfilled in more cases.

Comparing the A3 cases of the two tensile-strength laws (see Table 3), we can state that the formal averages of the output parameters do not significantly differ for the slope ratio, the size of the chunks, and the ice content of these chunks, respectively. However, regarding the mass outflows, the size-dependent tensile strength yields much more consistent data, with individual ratios around 2 and larger variations only for the CO_2 outflow rate (see also the inset of Fig. 10). For constant tensile strength, however, the H_2O outgassing rate seems to be somewhat smaller than for CO_2 and dust.

5.5 Correlations between the output and the input parameters

We can gain further insights into the physics of gas and dust emission, if we consider the correlations between the output and the input parameters. Fig. 12 shows, for the case of size-dependent tensile strength, the influence of the dust-to-ice ratio, the CO_2 content and the scale length of the tensile strength on the emission rates of H_2O, CO_2, and dust, the chunk size, the water-ice content of the emitted chunks, and the ratio of CO_2-to-H_2O-driven dust-emission events. The dust-to-ice ratio is clearly positively correlated with the water-emission rate, negatively correlated with the CO_2 emission rate, and mostly uncorrelated to the dust emission rate. The case is more complex for the correlation between the chunk size and the dust-to-ice ratio. Here, low and high dust-to-ice ratios yield larger chunks of up to ∼10 cm in size, whereas intermediate

dust-to-ice ratios around 5 result in chunk sizes hardly exceeding 1 cm. The water-ice content of the chunks is uncorrelated with the dust-to-ice ratio, and we found a negative correlation of the dust-to-ice ratio with the ratio of CO_2-to-H_2O-driven dust-emission events. In contrast, the CO_2 content seems not to have any significant influence on any of these output values, with the exception of the CO_2 outgassing rate and possibly also the dust emission rate. Finally, increasing the scale length of the tensile strength results in lower gas and dust emission rates and seems not to have any significant influence on the size and water-ice content of the chunks. The ratio of CO_2-to-H_2O-driven dust-emission events varies more for scale lengths between 1 and 3 cm than for 4 cm. In the case of 5 cm scale length, only a single case resulted in dust activity.

The input–output correlation in the case of constant tensile strength is shown in Fig. 13. There is a clearly visible distinction between dust-to-ice ratios of up to 5 and higher values. For the smaller dust-to-ice ratios, the dust-to-ice ratio has a positive correlation with all three gas and dust emission rates, no correlation to the H_2O- or CO_2-driven chunk size, a negative correlation to the ice content of the CO_2-driven chunks, and a negative correlation with the ratio of CO_2-to-H_2O-driven dust-emission events, respectively. For dust-to-ice ratios above 5, we only find a negative correlation between the dust-to-ice ratio and the CO_2 outgassing rate. All other output parameters seem not to be directly influenced by the dust-to-ice ratio. The size of the pebbles, a free parameter in the runs with constant tensile strength, is positively correlated with the size of the emitted chunks and uncorrelated to all other output parameters. Thus, the A3 solutions for constant tensile strength can only be found for relatively large pebbles (see Table 3), due to the deeper penetration of the radiation, which scales with pebble size. The CO_2 content only influences the CO_2-outgassing rate and the ratio of CO_2-to-H_2O-driven dust-emission events, but is basically uncorrelated to all other outputs. Finally, the value of the (constant) tensile strength shows a positive correlation with the
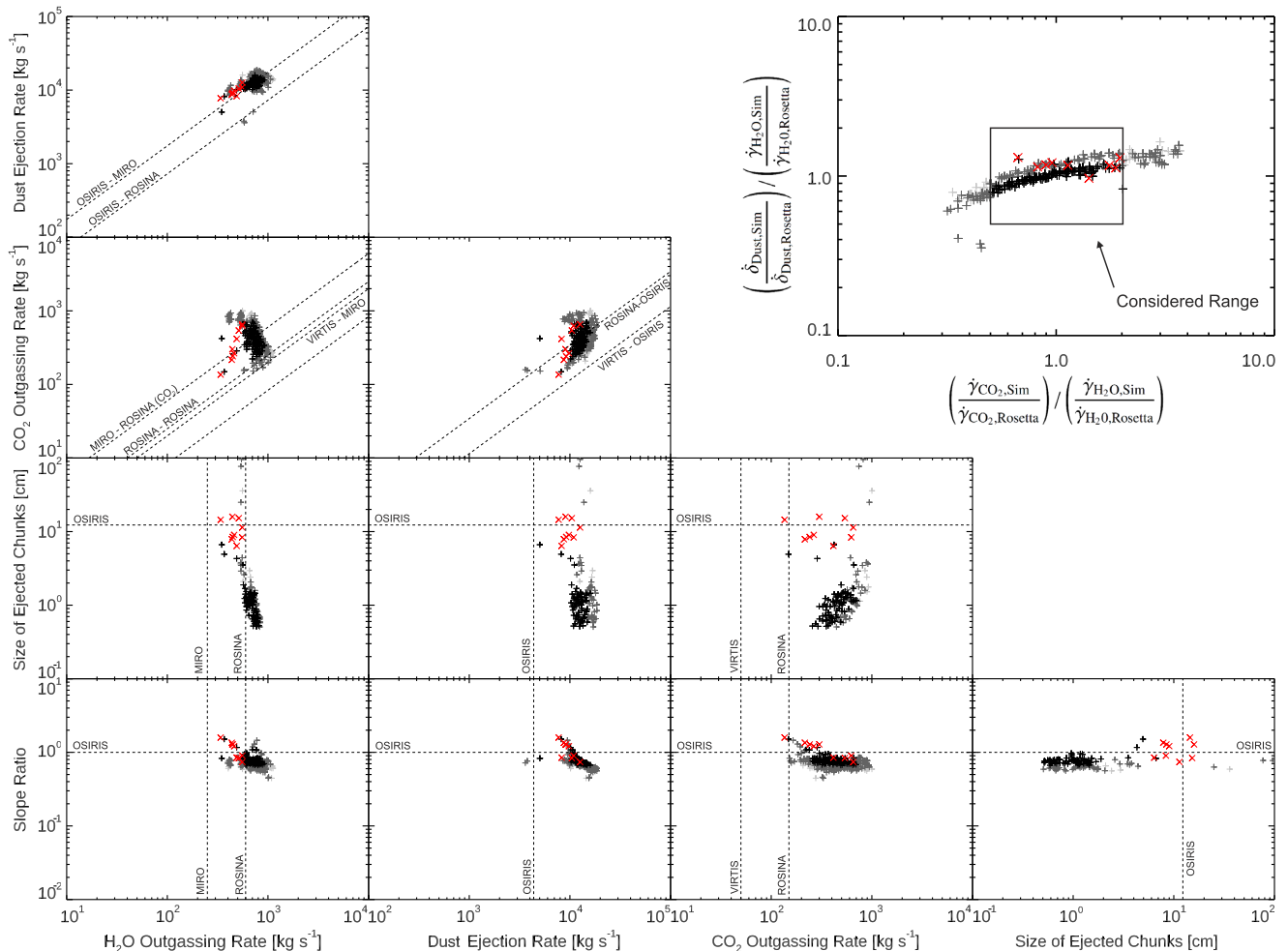
Figure 10. Summary of all resulting output parameters for the cases with size-dependent tensile strength (see Fig. 5 for details). The dashed lines denote the measured values by various Rosetta instruments, i.e. MIRO, ROSINA, VIRTIS, and OSIRIS (see Section 3). The best runs are identified by the three criteria discussed in the text and defined by equations (1)–(3) (A3), and are marked by the red crosses (see Table 3). One run possesses an infinite slope parameter (see Table 3), because only CO_2-driven events were detected. The size of the ejected chunks refers to the CO_2-driven ejection events, x_{CO_2}. The colours of the symbols denote the activity levels A3 (red), A2 (black), A1 (dark grey), and A0 (light grey), respectively.

H_2O emission rate and a positive-then-negative correlation with the other two gas and dust emission rates, with peak emissions in the 0.4–0.5 Pa range. The size of the CO_2-driven dust chunks has a positive correlation with tensile strength, whereas the size of the CO_2-driven dust seems to be uncorrelated with tensile strength. The ice content of the chunks is negatively correlated with the tensile strength, and the ratio of CO_2-to-H_2O-driven dust-emission events seem to be mostly uncorrelated to the tensile strength.

5.6 Histograms of the input parameters

To gain further insight into which of the input parameters determines the dust activity most, we plotted in Fig. 14 histograms of the activity levels as a function of dust-to-ice ratio (left), CO_2-ice content (centre), and scale length of the tensile strength (right), respectively, for the case of depth-dependent tensile strength. The white, light grey, dark grey, black, and red boxes denote, respectively, the number of NA, A0, A1, A2, and A3 events. For clarity, the y axis was plotted in logarithmic units. As already mentioned above, most of the active runs shown in Fig. 10 cluster very closely, but

fail to achieve the A3 activity level because of too small chunk sizes. However, these cases mostly belong to the A2 activity level (black boxes in Fig. 14) and can be used to show systematic trends. There is a clear maximum of likelihood for dust-to-ice ratios 4–6, a systematic increase of the occurrence of the A2 cases with increasing CO_2-ice content, and again a clear maximum for scale lengths of 2–4 cm. We produced similar histograms for the cases with constant tensile strength (see Fig. 15). Here, the distinction between the A3 and A2 activity levels stems mostly from a too high CO_2 outgassing rates in many cases (see Fig. 11). Also here, the A2 cases in Fig. 11 cluster closely together. The likelihood to achieve the A2 activity level is highest for dust-to-ice ratios 1–4, for CO_2-ice contents above 0.1, for tensile strengths between 0.3 and 0.7 Pa, and for pebble radii $\gtrsim 5$ mm (see Fig. 15).

6 DISCUSSION

This section aims at discussing the results of our work on matching the thermophysical model outcomes to the Rosetta observations at comet 67P.
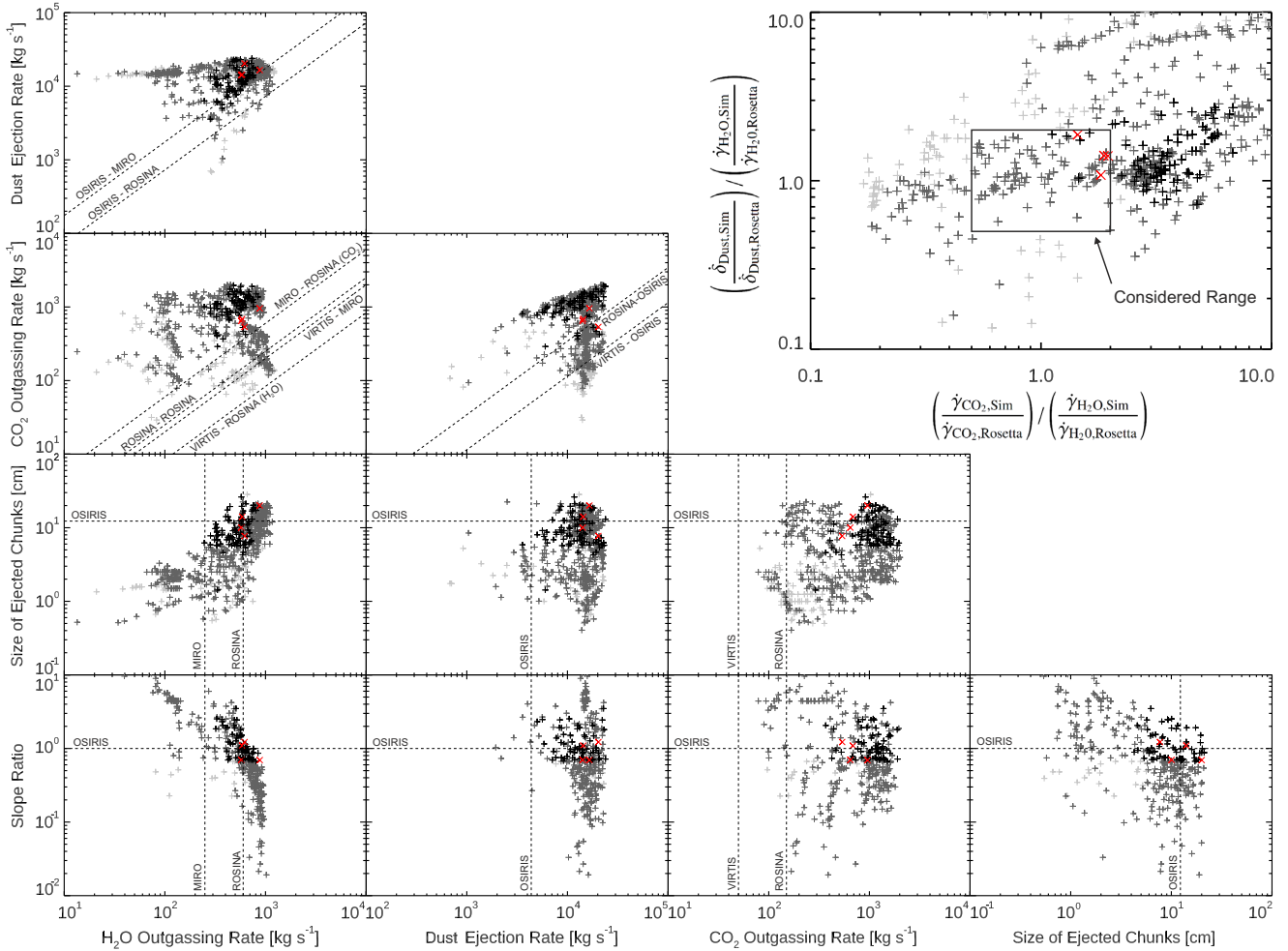
Figure 11. Summary of all resulting output parameters for the cases with constant tensile strength (see Fig. 5 for details). The dashed lines denote the measured values by various Rosetta instruments, i.e. MIRO, ROSINA, VIRTIS, and OSIRIS (see Section 3). The best runs are identified by the three criteria discussed in the text and defined by equations (1)–(3) (A3), and are marked by the red crosses (see Table 3). The size of the ejected chunks refers to the CO_2-driven ejection events, x_{CO_2}. The colours of the symbols denote the activity levels A3 (red), A2 (black), A1 (dark grey), and A0 (light grey), respectively.

6.1 Discussion of the simulation results

From the results shown in Figs 10–13, it becomes evident that the choice of our input parameters (see Table 2) encompasses values with which

(i) continuous dust and gas activity,

(ii) H_2O-gas emission rates exceeding the values measured by Rosetta,

(iii) CO_2-gas emission rates exceeding the values measured by Rosetta,

(iv) dust emission rates exceeding the values measured by Rosetta,

(v) H_2O/CO_2 ratios in gross agreement with Rosetta,

(vi) dust-to-gas ratios in gross agreement with Rosetta,

(vii) dust-chunk sizes in agreement with Rosetta, and

(viii) a slope of the size-frequency distribution function of the ejected dust in gross agreement with Rosetta (i.e. most of the dust mass is emitted in large chunks)

can be achieved. As far as we know, no other model has reached this result before.

6.1.1 Dust activity with depth-dependent tensile strength

As shown in Fig. 10, practically all simulated emission rates (H_2O, CO_2, dust) for the depth-dependent tensile strength exceed the values measured by the various Rosetta instruments. This is not a problem, because our extrapolation of a $1\,m^2$ of simulated area located exactly at the south pole point of comet 67P to a total of $10^7\,m^2$ of the illuminated Southern hemisphere naturally overestimates the total emission rates, because regions further away from the south pole possess different (and time-dependent) insolation patterns, which most likely lead on average to reduced activities for regions further away from the south pole. Moreover, not all of the Southern hemisphere has to be active at all. However, we circumvented this complication by choosing as one of the three activity criteria the mutual ratios between H_2O, CO_2, and dust activity (see Figs 10 and 11).

There is a clear positive correlation between the H_2O outgassing rate and the dust-to-ice ratio in the case of depth-dependent tensile strength (see Fig. 12). This counterintuitive behaviour (less ice produces more vapour) can be explained by a view on the other panels in the left-hand column of Fig. 12: with increasing dust-
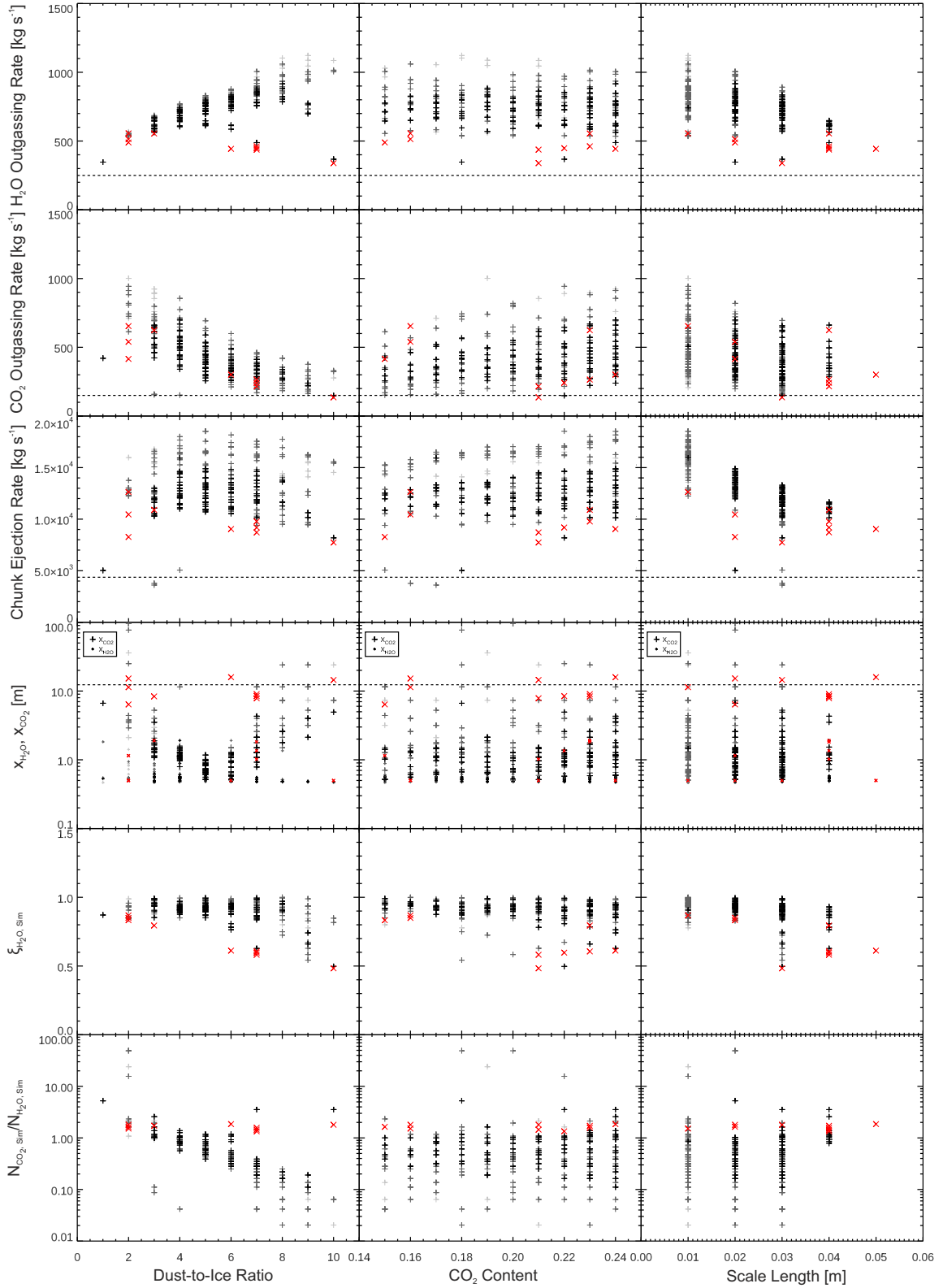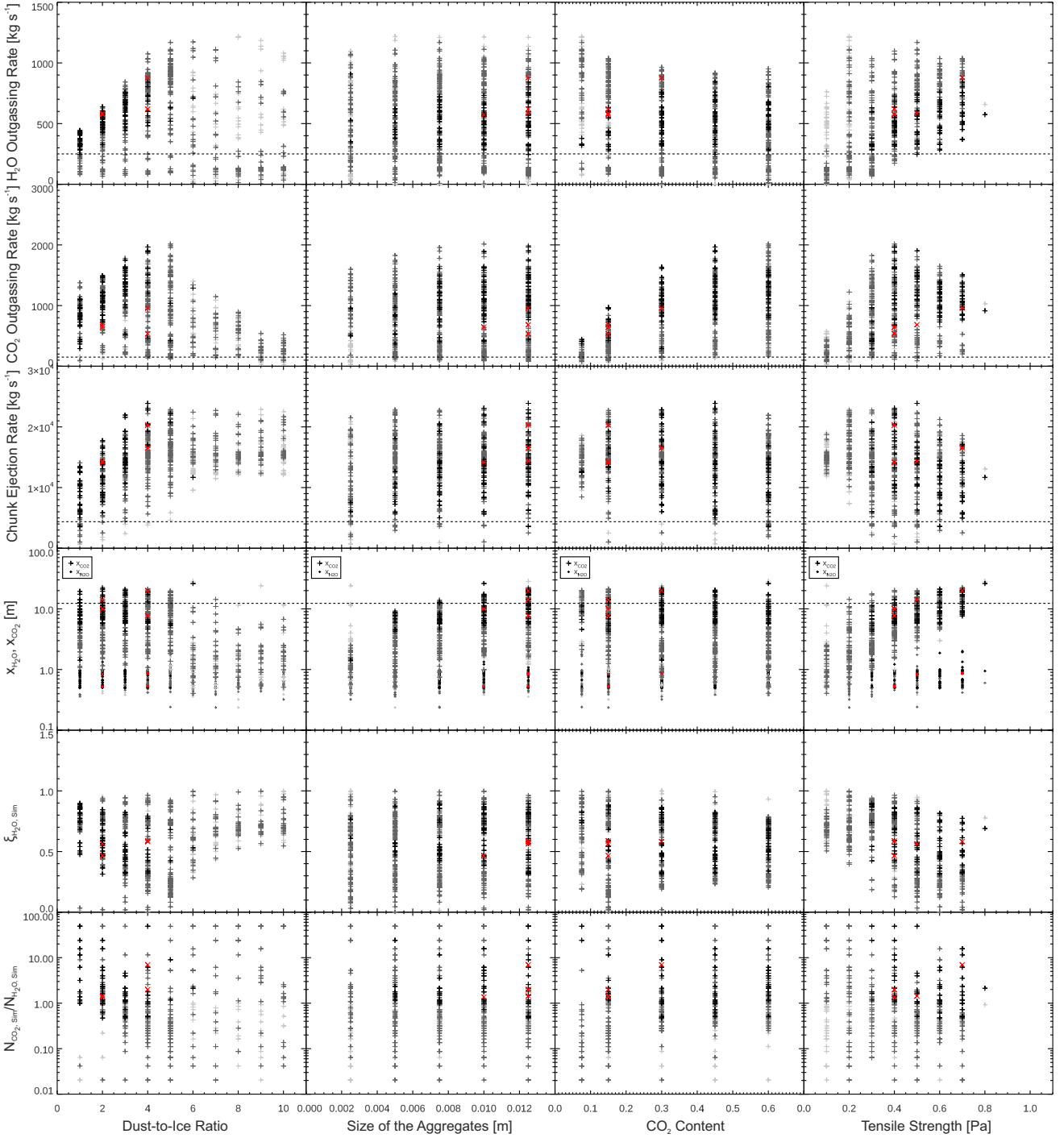
Figure 12. Summary of all input–output parameter correlations for a pebble surface, depth-dependent tensile strength, and low gas permeability (see Fig. 5 for details). The dashed lines visualize the Rosetta measurements (see Section 3). In addition, also the ratio of ejection events driven by CO_2 and H_2O activity, $N_{CO_2, Sim}/N_{H_2O, Sim}$, is shown. Please note that for the $x_0 = 5$ cm run, only CO_2-driven ejection events were found (no data point for x_{H_2O} and $N_{CO_2}/N_{H_2O} = \inf$). The colours of the symbols denote the activity levels A3 (red), A2 (black), A1 (dark grey), and A0 (light grey), respectively.

Figure 13. Summary of all input–output parameter correlations for a pebble surface, constant tensile strength, and low gas permeability (see Fig. 5 for details). The dashed lines visualize the Rosetta measurements (see Section 3). In addition, also the ratio of ejection events driven by CO_2 and H_2O activity, $N_{CO_2, Sim}/N_{H_2O, Sim}$, is shown. The colours of the symbols denote the activity levels A3 (red), A2 (black), A1 (dark grey), and A0 (light grey), respectively.

to-ice ratio, the ratio between CO_2-driven and H_2O-driven chunk ejection decreases. As the total dust ejection rate is more or less independent of the dust-to-ice ratio, this means that the contribution through H_2O-driven chunk ejection increases with increasing dust-to-ice ratio and, thus, determines more and more the H_2O–vapour emission rate, as observed in the simulations. It should be noted that dust chunks emitted through H_2O activity are completely devoid of H_2O ice. Likewise, CO_2-driven dust activity produces

chunks completely devoid of CO_2 ice, but only partially depleted in H_2O ice (see Fig. 12). However, the CO_2 emission rate decreases with increasing dust-to-ice ratio and, thus, with decreasing CO_2–ice content, because the importance of the CO_2-driven dust emission decreases, as the bottom left-hand panel of Fig. 12 shows. Thus, inferring dust-to-ice ratios from measured gas and dust emission rates is not as straightforward as one might assume, but requires excessive thermophysical modelling.
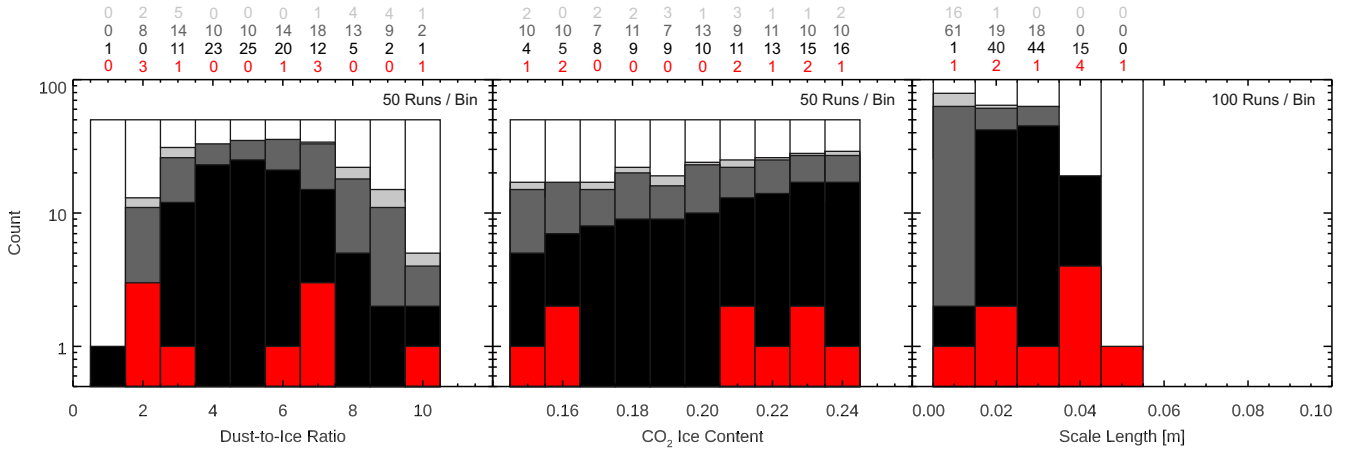
Figure 14. Histogram of the input parameters required for reaching activity level A3 (red), A2 (black), A1 (dark grey), A0 (light grey), or NA (white) for the depth-dependent tensile strength. The numbers above each bin indicate the numbers of simulated events in the respective activity level. Please mind the logarithmic units of the ordinate.
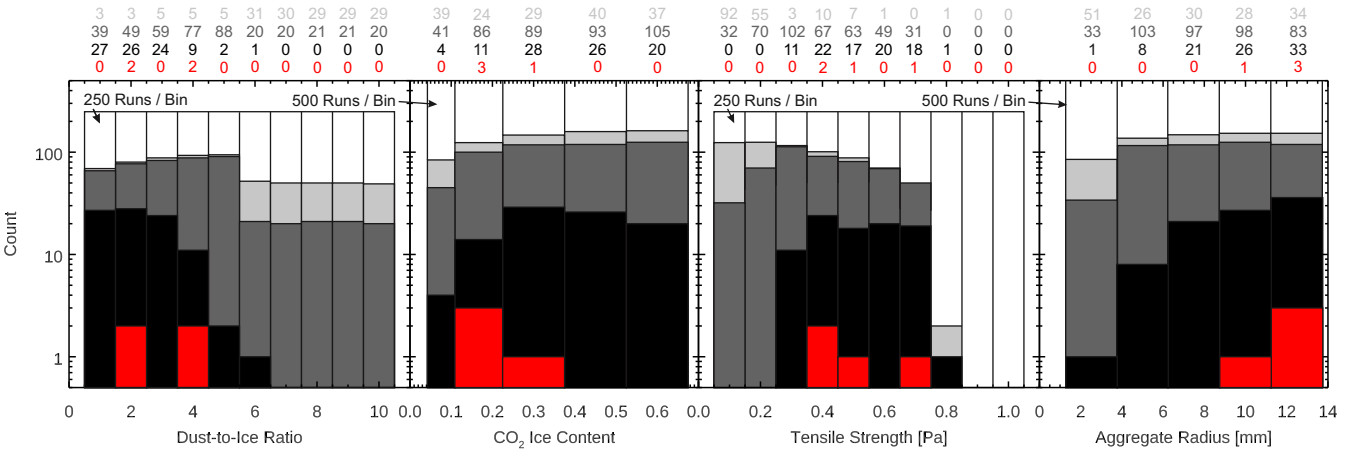

Figure 15. Histogram of the input parameters required for reaching activity level A3 (red), A2 (black), A1 (dark grey), A0 (light grey), or NA (white) for the constant tensile strength. The numbers above each bin indicate the numbers of simulated events in the respective activity level. Please mind the logarithmic units of the ordinate.

The biggest difference between the Rosetta observations and the results of the thermophysical model in the case of depth-dependent tensile strength is the size of the CO_2-driven dust chunks. Fig. 12 shows that sufficiently large chunks to match the Rosetta observations are achieved for dust-to-ice ratios scattered between 2 and 10, whereas the CO_2 content and the scale length of the tensile strength do not play a major role for the chunk size.

6.1.2 Dust activity with constant tensile strength

Also in the case of constant tensile strength, most of the simulated emission rates (H_2O, CO_2, dust) are higher than the measured ones (Fig. 11, see also Section 6.1.1). But why is the CO_2-emission rate excessively high? The answer is that the importance of CO_2-driven dust activity is much higher for constant tensile strengths than for the depth-dependent tensile strength (compare Fig. 13 to Fig. 12), due to the assumed σ_0 value in the depth-dependent tensile strength case (increasing σ_0 could lead to ejection of larger chunks). There are also cases in which the dust activity is exclusively driven by CO_2 (in this case, we replaced $N_{CO_2,Sim}/N_{H2O,Sim} = \infty$ by $N_{CO_2,Sim}/N_{H2O,Sim} = 50$ in Fig. 13). As dust emission always occurs

at the interface between ice-free and ice-containing layers, these chunks are completely devoid of CO_2, but still contain considerable amounts of H_2O ice (see Fig. 13). Thus, the emission of CO_2 vapour is enhanced relative to H_2O vapour.

Besides a CO_2 emission rate that is on average a factor $\sim$3 too high (see inset in Fig. 11; cases A2), the other criteria match well the Rosetta results. Most of the ejected chunks have sizes around 10 cm and the slope of the size-distribution function is only slightly below the inferred Rosetta value (see Fig. 11). Fig. 15 shows that dust-to-ice ratios from 2 to 4, CO_2-ice contents from 0.1 to 0.4, tensile strength values of 0.4–0.7 Pa and pebble radii $R > 4$ mm are the favourable input parameters. Following the tensile-strength model for pebbles by Skorov & Blum (2012)

$$\sigma_T \approx 0.5 \, \text{Pa} \left(\frac{R}{1 \, \text{mm}} \right)^{-2/3}, \tag{4}$$

we get for the above tensile strengths pebble radii in the range $R = 0.6$–2.2 mm if the dominating pebble material would be SiO_2. Thus, it seems that the pebbles in comet 67P consist of a material that is somewhat more cohesive than SiO_2. All in all the retrieved pebble sizes and tensile strength are not inconsistent.
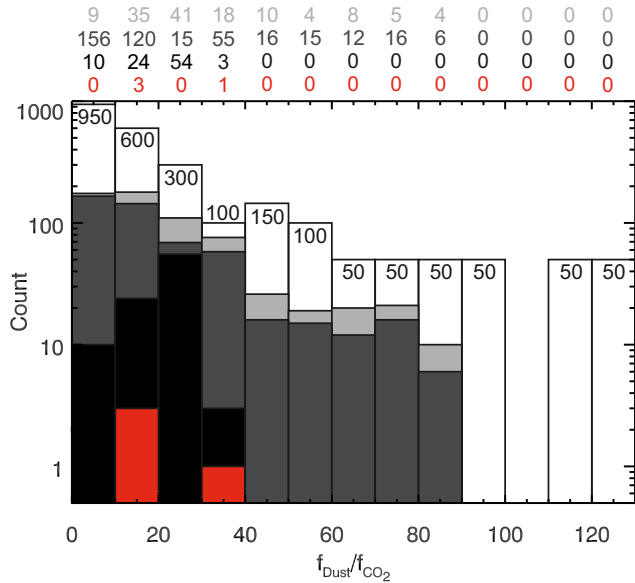
Figure 16. Histogram of the number of occurrences of activity levels NA (white), A1 (light grey), A2 (dark grey), A2 (black), and A3 (red), respectively, as a function of the dust-to-CO_2-ice ratio. Mind that for better visibility, the ordinate is shown in logarithmic units. The numbers above the plot show, with identical colours, the number of events with activity levels A0, A1, A2, and A3, respectively. The total number of runs per bin is shown at the upper end of the white bar.

6.1.3 No-pebble case

For the no-pebble case, we assumed that the thermal conductivity is constant ($\lambda = 10^2$ W m^{-1} K^{-1} or $\lambda = 10^3$ W m^{-1} K^{-1}). Furthermore, the porosity is given by the smallest particle structure, i.e. $r = 1$ μm. This implies that the volume filling factor is 0.4 and that α in equation (A25) must be computed by using the particle radius, $r = 1$ μm, instead of the pebble radius, R (this parameter is not relevant in the no-pebble case).

This has the implication that the outgassing rate is much higher and, hence, the sublimation front can be found at greater depths. However, at greater depths, the temperature is lower and pressures of 0.1 to 1.0 Pa cannot be reached. Hence, no continuous dust eject was observed for the no-pebble case.

6.1.4 Role of dust-to-ice ratio and CO_2 content

Besides the positive correlation between the dust-to-ice ratio and the water–vapour outgassing rate discussed above, the water–ice content plays another role. In case of a high dust-to-ice ratio, energy losses due to conversion into latent heat are smaller and, thus, cooling is less efficient. Hence, the temperature in the layers is generally higher for higher dust–ice ratios and more molecules can sublimate per second, which leads to faster ejection time-scales. In contrast, an increase of the dust-to-ice ratio has also the consequence of a lower CO_2 outgassing rate, because the faster sublimation rate depletes the CO_2 ice in the first layers very fast. Later, but before the ejection event occurs, the CO_2 ice is buried beneath a covering dust layer, which leads to a reduction of the outgassing rate.

The direct role of the CO_2–ice content on the activity can be seen in Fig. 16 where the occurrences of the different activity levels are plotted in histogram form as a function of the dust-to-CO_2-ice ratio. Similar to the case with water ice (see Fig. 15), the overall activity likeliness (i.e. the fraction of runs with dust activity of any

level to the total number of runs) is independent of the dust-to-CO_2-ice ratio. However, the likelihood of the higher activity level A2 clearly peaks for dust-to-CO_2-ice ratios of 20–30. Although this might look like a bias of our activity-level definition (see Section 5), which favours dust-to-CO_2-ice ratios around the value 29 measured for comet 67P, but a comparison to the inset of Fig. 11 shows that a large number of A2 events fall outside the factor of two window allowed by the definition. Thus, we think that dust-to-CO_2-ice ratio around 20–30 favour the emission of large chunks in such quantities that they dominate the size–frequency spectrum.

6.1.5 Role of diffusion length

As described in Section 4, we tried two permeability coefficients, $b = 1$ pd and $b = 7$ pd, respectively. As can be seen in Fig. 5, none of the $b = 7$ pd runs led to any dust activity. The reason for this behaviour is that the larger diffusion lengths in the $b = 7$ pd case lead to a better escape of the gas from deeper layers and, thus, to a much lower pressure at these depths (see Fig. 6). In none of the $b = 7$ pd cases, the pressure exceeded the lower limit of $\sigma_T = 0.1$ Pa set for our simulations.

6.1.6 Role of back diffusion

The back diffusion has only a minor influence on the simulation results. We tested the role of back diffusion by performing exactly the same runs as shown in Table 3 (red cases; A3), but with back diffusion disabled. Disabling the back diffusion has the consequence that no energy is transported into deeper layers by the gas molecules. Consequently, latent cooling of the active layers is less effective and higher pressures can be reached.

The obtained results without back diffusion are shown by the italic numbers in Table C1. It can be seen, by comparing the black numbers (runs with back diffusion) with the italic numbers (runs without back diffusion) that the calculated outgassing rates, dust ejection ratios, slope ratios, and ice contents deviate by less than 15 per cent to the original runs. Furthermore, disabling back diffusion generally decreases the size of the large chunks, because higher pressures can be reached in shallower depths since the latent heat cooling rate is decreased (see above).

6.1.7 Water–ice content of the ejected chunks

Fig. 12 shows that the water–ice content of the chunks emitted due to CO_2 outgassing is typically $\xi_{H2O, Sim} \approx 0.8 - 1$ in the case of depth-dependent tensile strength, more or less independent of the input parameters. For constant tensile strength, we find a much wider range of water–ice contents of $\xi_{H2O, Sim} \approx 0.1 - 0.9$, with the widest range for dust-to-ice ratios of 3–5 and somewhat higher values for smaller and larger dust-to-ice ratios (see Fig. 13). As already mentioned above, these strong variations in ice content of the emitted chunks mean that the measured H_2O/CO_2 outgassing ratio is by no means indicative of the H_2O/CO_2–ice content inside the comet nucleus.

6.2 Important notes

Analysis of our thermophysical model yields a variety of aspects that shall be addressed in the following.

(i) A thermal conductivity that is driven by radiative transport (i.e. $\lambda \propto T^3$, which dominates the heat conductivity in the pebble model),

leads to the development of convex-shaped temperature profiles above the water–ice sublimation front, in contrast to a temperature-independent heat conductivity, which leads to a concave shape (see Fig. 7b). As a result, the temperature profile is rather flat at the surface in the pebble case as compared to the homogeneous cases.

(ii) Latent heat cooling is a major energy sink that significantly cools the active layers (see kinks in the temperature profile shown in Fig. 7b). This has several consequences: (1) the sublimation front needs longer to reach deeper layers and the time-scale for example for the dust ejection increases, (2) the sublimated molecules can transport the energy into deeper layers where the deposition leads to a temperature increase, which directly affects the energy transport in these layers (Fourier's law), (3) a loss of the cooling process leads to a significant increase of the layer's temperature.

(iii) Because of the complex dependence of the outgassing and dust ejection rates on the dust-to-H_2O–ice ratio, as explained above, one further conclusions is that the dust-to-H_2O–vapour ratio in the lost mass of comets is not a reasonable measure for the dust-to-H_2O–ice content of the near-surface layers. The deduction of the dust-to-H_2O–ice ratio requires the usage of a thermophysical model that takes the microphysical properties of the cometary surface layers into account.

(iv) Smaller tensile strengths (used as input parameter) lead to higher dust ejection rates and smaller sizes of the ejected chunks (see Fig. 13). As Fig. 8 shows, this is because lower gas pressures can be reached both by H_2O and CO_2 outgassing at relatively shallow depths.

(v) With each ejection event, fresh material is directly illuminated by the Sun (see e.g. Rinaldi et al. 2018; Tubiana et al. 2019). The outgassing rates are high immediately after an ejection event and thereafter decrease with time, because of the increase of the covering dust layer thickness, until another ejection event occurs. Hence, the ejection rate, the size of the chunks, and the ratio of the H_2O-driven to the CO_2-driven ejection events strongly affect the outgassing rates.

(vi) To simultaneously fulfil all three success criteria defined in Section 5 in a single simulation is very difficult. Only 9 out of 500 runs for the size-dependent tensile strength and only 4 out of 2500 runs for the constant tensile strength matched all three criteria (see Table 3; but mind that the initial dust-to-CO_2–ice ratios were out of the Rosetta range in many simulations). A comparison of the runs of the two different tensile-strength laws (length dependent versus constant) shows that the ratios of the gas- and dust-emission rates are better matched with a depth-dependent tensile strength, whereas the chunk sizes of the constant tensile strength model are closer to the Rosetta observations. The slope of the size distribution function seems not to be a major problem, because in most simulations, much more mass is emitted through CO_2 activity than through H_2O activity.

6.3 The role of fallback on the Northern hemisphere

During perihelion, the Southern hemisphere of comet 67P received maximum illumination, whereas the Northern hemisphere remained in darkness. Because of the CO_2–ice richness of the south, CO_2-driven activity was able to eject large dust chunks, which contained considerable amounts of their original H_2O–ice content, as shown here in this paper. That CO_2-driven activity can eject large water–ice chunks was already observed during the flyby of the EPOXI mission at comet Hartley 2 (A'Hearn et al. 2011).

Besides CO_2-driven dust activity, the Southern hemisphere also emitted ice-free dust due to H_2O outgassing, but these latter particles

were essentially individual pebbles, as Figs 12 and 13 show. While the emission of large chunks cannot set a large number of fractal particles free, the ejection of individual pebbles provides the basis for the release of all interstitial fractal aggregates (Fulle & Blum 2017). Hence, the ratio of small-to-large chunks determines the emission of fractal dust aggregates, which could be collected by GIADA and MIDAS.

Large chunks that, after lift-off from the southern regions of comet 67P, are on trajectories directed towards the Northern hemisphere may ultimately fall back on to the nucleus, due to the absence of lifting force in these regions. Hence, the Northern hemisphere accumulates solid material around perihelion that originates from the southern regions. An indication for the mass accumulation is provided by measuring the shadows of boulders in the Hapi region (see the upcoming paper by P. Cambianica). As mentioned above, the large chunks contain considerable amounts of their initial H_2O ice, but no CO_2 ice, because the chunks were ejected due to CO_2 sublimation. Thus, the Northern hemisphere accumulates surface material composed of non-volatile dust and H_2O ice. When the Sun returns to the northern regions of the comet, dust activity can resume, but the ejected particles will most likely not contain large chunks. Moreover, gas activity in the Northern hemisphere should be dominated by H_2O.

6.4 The role of fallback on the Southern hemisphere

It is natural to expect also some fallback of dust on the Southern hemisphere, although the steady gas flow streaming out of the southern regions around perihelion should make this more difficult. However, as our data show that the largest chunks, which might be the easiest to re-deposit in the south of comet 67P, contain a non-negligible amount of H_2O ice, this material might still be active, leading to the ultimate re-emission of all pebbles and the total amount of H_2O vapour contained in the chunks into space. However, the re-accumulation of ejected dust might be rare, due to the strong lifting force on the Southern hemisphere. On top of that, the steep positive slope of the size–frequency distribution between pebble and kg-chunk sizes (see Section 5) shows that re-deposition of dust on the Southern hemisphere cannot be very significant, because it would enhance the mass in the pebble bin relative to the kg-chunk bin, which is not observed.

6.5 The largest comet able to eject 1 kg heavy chunks

To assess whether dust ejection is possible, we made the assumption that the gravitational pull of the comet nucleus is negligible with respect to the gas pressure. While this assumption is valid for comet 67P for the dust sizes observed, the gravitational pressure of the chunks increases for larger comets. In order to derive the largest chunk size x_{Max} that can be detached off a cometary surface (with the same properties and under the same conditions as the Southern hemisphere of comet 67P at perihelion), we can formulate the condition that the lithostatic pressure of the chunks equals the tensile strength of the surface (**when the lithostatic pressure is higher than the tensile strength, dust activity is not possible anymore**),

$$\rho_{Chunk} \, g \, x_{Max} = \sigma_T. \quad (5)$$

Here, ρ_{Chunk} and g are the bulk mass density of the chunk and the gravitational surface acceleration of the comet, respectively. With the definition of the gravitational acceleration, this equation can be
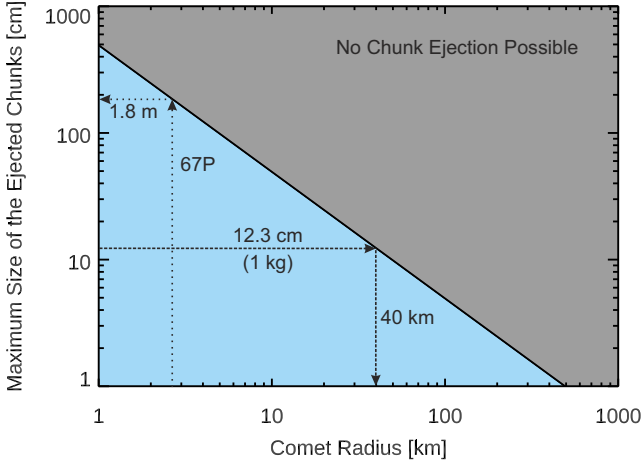
Figure 17. Maximum chunk size that can be detached off a cometary surface as a function of the radius of the nucleus (see equation 6). For these calculations, we assumed $\rho_{Comet} = \rho_{Chunk} = 532\,kg\,m^{-3}$ and $\sigma_T = 0.4\,Pa$. The maximum nucleus radius that is able to eject 1 kg heavy chunks is $R_{Comet} = 40\,km$. Comet 67P is able to eject chunks with sizes up to $\sim 2\,m$.

reformulated into

$$x_{Max} = \frac{3}{4\pi} \frac{\sigma_T}{\rho_{Chunk}\,\rho_{Comet}\,\gamma} \frac{1}{R_{Comet}} \approx \frac{3}{4\pi} \frac{\sigma_T}{\rho_{Chunk}^2\,\gamma} \frac{1}{R_{Comet}}, \quad (6)$$

where γ is the gravitational constant, R_{Comet} is the radius of the nucleus, and $\rho_{Comet} \approx \rho_{Chunk}$ is its mass density. Fig. 17 shows the resulting maximum chunk sizes that can be detached from different sized cometary nuclei for a tensile strength of 0.4 Pa (solid line). For example, the maximum nucleus radius capable to eject 1 kg heavy chunks is $R_{Comet} = 40\,km$. Comet 67P is able to eject chunks up to sizes of 1.8 m. Large chunks have been observed close to the nucleus of 67P. For example, Agarwal et al. (2016) tracked chunks up to 1.6 m in size[5] (diameter). Furthermore, the largest chunk found by Fulle et al. (2016) measures 0.8 m.

It is important to note that this approach only describes the condition for lift-off. Any gas–dust interaction and the dynamics of the chunks in the inner coma are not discussed by this approach. Also, whether the required gas pressure can be built up at the respective depths is also not discussed by this simple approach.

6.6 Do fractal aggregates between the pebbles change this picture?

Fulle & Blum (2017) showed that the measurements of extremely fluffy dust particles by the GIADA and MIDAS instruments onboard *Rosetta* can be explained by the capture of these agglomerates between the pebbles during the formation stage of the planetesimal from which the comet nucleus originated. Gentle collisions after the formation stage by which the comet nucleus gained its current size and shape should also not affect the fluffy dust (Schwartz et al. 2018). The question is now whether these fluffy particles, so far neglected in our simulations, would cause problems with the picture shown in this paper.

Following measurements of the MIDAS instrument onboard *Rosetta*, dust aggregates consist of monomer grains with typical

---

[5]The values are taken from the Agarwal et al. (2016) paper (Fig. 8), converted into size (diameter), and corrected by a factor 4.4 (see footnote number 3 in Güttler et al. (2019)).

sizes of $s_g \approx 100\,nm$ (Mannel et al. 2019). Following Fulle & Blum (2017), the dust particles between the pebbles have radii of up to $s_f \approx 4\,mm$. Assuming a fractal dimension of $D_f = 1.4$ (Krause & Blum 2004), we get the number of monomer grains inside a fractal particle $N = (s_f/s_g)^{D_f} = 2.8 \times 10^6$. The geometric depth of this fractal particle is given by the total cross-section of all monomers divided by the area occupied by the fractal particle, $\tau_g = N s_g^2/s_f^2 = (s_g/s_f)^{2-D_f} = 1.7 \times 10^{-3}$. Thus, molecules diffusing through the matrix of pebbles will not be interacting with interstitial fractal particles. Moreover, the radiative heat transport from pebble to pebble will also not be affected by these particles, because the thermal wavelengths at the typical temperatures of 100–300 K are 10–30 μm, which is a factor 100–300 larger than the monomer grains so that electromagnetic interaction is extremely inefficient.

7 SUMMARY

Our thermophysical model (see Appendix A) is the first simulation capable of explaining the continuous dust ejection from the surface of a cometary nucleus. Based on this model, we can infer the following conclusions about the properties of the Southern hemisphere of comet 67P:

(i) Comet 67P consists of pebbles (dust aggregates), which indicates that the comet (or its precursor planetesimal) formed by the gentle gravitational collapse of a pebble cloud. The pebble size has been estimated in earlier work to be 3–6 mm in radius (Blum et al. 2017). In this work, we cannot well constrain the pebble size, but our results indicate that the required radii are at least in the above range, although the length-independent tensile strength requires systematically larger pebbles. All no-pebble cases have shown no dust ejection, because the sublimation front was located at greater depths and, hence, pressures above 0.1 Pa were never reached.

(ii) The sublimation of CO_2 ice drives the ejection of H_2O-ice-containing large (dm-sized) dust chunks, whereas the sublimation of H_2O ice causes the emission of dry and smaller (cm-sized) chunks or individual pebbles, which however have no signature in the size distribution observed by *Rosetta*.

(iii) Assuming that pebbles sample the sub-cm dust observed by *Rosetta* (characterized by a continuous size distribution), the size–frequency distribution observed by *Rosetta* can be matched by our simulations, although most runs end at flatter positive slopes.

(iv) Mass-loss rates of H_2O, CO_2, and dust in most simulation runs exceed those observed by the *Rosetta* instruments, but their ratios are compatible to those observed. The higher simulated rates can either be explained by inactive areas or by the extrapolation from the south pole to the entire Southern hemisphere of comet 67P, which naturally overestimates the activity. Future work needs to address this point by adopting our thermophysical model to a shape model of comet 67P.

(v) Depending on the tensile-strength model, the large chunks still contain 10–90 per cent of their initial H_2O ice. The chunks may fall back on to the Northern hemisphere of comet 67P where they lead to the outgassing of H_2O vapour and the emission of ice-free small dust chunks or single pebbles.

(vi) We find good agreement between *Rosetta* observations and model predictions for both cases of tensile strengths, i.e. for a depth-dependent and a constant tensile strength. However, most of the simulations for the depth-dependent tensile strength predict too small chunks, whereas most of the simulations with constant tensile strength predict too high CO_2 outgassing rates. Typical tensile-

strength values at the emission of chunks are in the range of 0.3–0.7 Pa, in good agreement with the Rosetta results presented by Attree et al. (2018).

(vii) The dust-to-ice ratios required to explain the emission of dm-sized dust chunks are ranging from 2 and 10 (red bars in Figs 14 and 15).

(viii) Furthermore, the dust-to-ice ratio controls the ratio of CO_2-driven to H_2O-driven ejection events. With decreasing water–ice content, more H_2O-driven ejection events were observed, independent of the tensile-strength law.

(ix) The outgassing rate of water vapour depends on the dust-to-ice ratio. For higher dust-to-ice ratios, the H_2O outgassing rate increases. Thus, the dust-to-H_2O-gas ratio in the lost material is not a measure of the dust-to-H_2O-ice ratio in the comet nucleus, because H_2O ice can leave the comet inside the large dust chunks.

(x) Inward diffusion of volatiles is an important process and must not be ignored in thermophysical models, because the corresponding transport of latent heat has a significant impact on the temperature stratification beneath the respective ice layers.

(xi) Our simulations do not allow us to constrain the CO_2–ice content. However, the dust-to-CO_2-gas ratio measured in the coma is a good proxy for the dust-to-CO_2-ice ratio inside the comet.

(xii) A low gas permeability (or gas diffusivity) is required to allow a pressure build-up high enough to exceed the tensile strength of the material and, therewith, to allow dust ejection (see Fulle et al. 2019).

(xiii) Due to the simplicity of our approach, we cannot at this stage constrain the active area fraction of the Southern hemisphere of comet 67P. 3D simulations using a shape and illumination model are, thus, required.

(xiv) Based on our simulations we can infer that the largest comet capable to eject dust chunks with masses in the kg-regime measures 40 km in radius. Comet 67P can in principle eject up to $2-m$ sized chunks.

(xv) It is important to note that thermophysical models with the aim to model the temperature stratification as well as dust and gas activity of cometary nuclei must implement the following concepts: (i) at least two volatile species, (ii) radiative and conductive thermal transport, (iii) latent-heat cooling and transport and (iv) gas diffusion.

(xvi) A possibility to further increase the size of the ejected chunks is to use larger values for σ_0 in the depth-dependent tensile strength case. However, this investigation will be a task of a future publication.

ACKNOWLEDGEMENTS

REFERENCES

A'Hearn M. F. et al., 2011, Science, 332, 1396
Agarwal J. et al., 2016, MNRAS, 462, S78
Attree N. et al., 2018, A&A, 611, A33
Bažant Z. P., 1999, Arch. Appl. Mech., 69, 703
Bertaux J.-L., 2015, A&A, 583, A38
Blum J., 2018, Space Sci. Rev., 214, 52
Blum J., Gundlach B., Mühle S., Trigo-Rodriguez J. M., 2014, Icarus, 235, 156
Blum J. et al., 2017, MNRAS, 459, S755
Brisset J., Heißelmann D., Kothe S., Weidling R., Blum J., 2016, A&A, 593, A3
Bryson C., Cazcarra V., Levenson L. L., 1974, J. Chem. Eng. Data, 19, 107
Chan C. K., Tien C. L., 1973, J. Heat Trans., 95, 302
Davidsson B. J. R., Skorov Y. V., 2002, Icarus, 159, 239
Davidsson B. J. R. et al., 2016, A&A, 592, A63
Fougere N. et al., 2016, MNRAS, 462, S156
Fulle M., Blum J., 2017, MNRAS, 469, S39
Fulle M., Blum J., Rotundi A., 2019, ApJ, 879, L8
Fulle M., Blum J., Rotundi A., Gundlach B., Güttler C., Zakharov V., 2020, MNRAS, 476
Fulle M. et al., 2016, ApJ, 821, 19
Gundlach B., Blum J., 2012a, Icarus, 219, 618
Gundlach B., Blum J., 2012b, Icarus, 219, 618
Gundlach B., Skorov Y. V., Blum J., 2011, Icarus, 213, 710
Gundlach B. et al., 2018, MNRAS, 479, 1273
Güttler C. et al., 2019, A&A, 630, A24
Hansen K. C. et al., 2016, MNRAS, 462, S491
Heim L.-O., Blum J., Preuss M., Butt H.-J., 1999, Phys. Rev. Lett., 83, 3328
Hu X. et al., 2017, A&A, 604, A114
Johansen A., Oishi J. S., Mac Low M.-M., Klahr H., Henning T., Youdin A., 2007, Nature, 448, 1022
Jorda L. et al., 2016, Icarus, 277, 257
Keller H. U. et al., 2015, A&A, 583, A34
Keller H. U. et al., 2017, MNRAS, 469, S357
Krause M., Blum J., 2004, Phys. Rev. Lett., 93, 021103
Lorek S., Lacerda P., Blum J., 2018, A&A, 611, A18
Läuter M., Kramer T., Rubin M., Altwegg K., 2019, MNRAS, 483, 852
Mannel T., Bentley M. S., Schmied R., Jeszenszky H., Levasseur-Regourd A. C., Romstedt J., Torkar K., 2016, MNRAS, 462, S304
Mannel T. et al., 2019, A&A, 630, A26,
Marshall D. W. et al., 2017, A&A, 603, A87
Mavko G., Meukerji T., Dvorkin J., 2009, The Rock Physics Handbook: Tools for Seismic Analysis of Porous Media. Cambridge Univ. Press, Cambridge
Merrill B., 1969, Nasa Technical Note, TN, D
Orosei R., Capaccioni F., Capria M. T., Esinasse S., Federico C., Salomone M., Schwehm G. H., 1995, A&A, 301, 613
Ott T. et al., 2017, MNRAS, 469, S276
Petrenko V., Whitworth R., 1988, Europhys. News, 19, 61
Prialnik D., Sarid G., Rosenberg E. D., Merk R., 2008, Space Sci. Rev., 138, 147
Prialnik D., Sierks H., 2017, MNRAS, 469, S217
Rinaldi G. et al., 2018, MNRAS, 481, 1235
Schwartz S. R., Michel P., Jutzi M., Marchi S., Zhang Y., Richardson D. C., 2018, Nat. Astron., 2, 379
Sierks H. et al., 2015, Science, 347, aaa1044
Skorov Y. V., Blum J., 2012, Icarus, 221, 1
Skorov Y. V., Rezac L., Hartogh P., Bazilevsky A. T., Keller H. U., 2016, A&A, 593, A76
Skorov Y. V., v. Lieshout R., Blum J., Keller H. U., 2011, Icarus, 212, 867
Tubiana C. et al., 2019, A&A, 630, A23
Weidling R., Guettler C., Blum J., 2012, Icarus, 218, 688
Weidling R., Guettler C., Blum J., Brauer F., 2009, ApJ, 696, 2036
Weissman P., Morbidelli A., Davidsson B., Blum J., 2019, Space Sci. Rev., 216, 6
Windmark F., Birnstiel T., Güttler C., Blum J., Dullemond C. P., Henning T., 2012, A&A, 540, A73
Womack M., Sarid G., Wierzchos K., 2017, PASP, 129, 031001
Youdin A. N., Goodman J., 2005, ApJ, 620, 459
Zsom A., Ormel C. W., Güttler C., Blum J., Dullemond C. P., 2010, A&A, 513, A57

SUPPORTING INFORMATION

Supplementary data are available at *MNRAS* online.

Fig. 8. Example of a run with with repeated dust activity.

Please note: Oxford University Press is not responsible for the content or functionality of any supporting materials supplied by the authors. Any queries (other than missing material) should be directed to the corresponding author for the article.

APPENDIX A: THE THERMOPHYSICAL MODEL

Here, we give a detailed description of the thermophysical model and organize it in the following sections according to the blocks shown in Fig. 3 of the main text. Table A1 summarizes all parameters used in this work.

A1 1st block: thermal conduction and outgassing

The first block solves the heat transfer equation based on the thermal conductivity, $\lambda(T)$, and the efficiency function, $\eta(x)$, as shown in the following. For simplicity, we write $T(x)$ instead of $T''(x)$ for the temperature (see Fig. 3), but it is important to keep in mind that the thermal conductivity calculation is based on the temperature profile from the prior time-step.

A1.1 Heat transport, $\lambda(T'')$

The transfer of thermal energy from one layer to another is driven by three different transport processes, namely by conduction through the solid particle contacts (network conduction), by radiation (radiative transfer), and by sublimation and condensation of molecules (latent heat transport). The latter is calculated in the last block of the thermophysical model (see Appendix A3).

The network thermal conductivity of granular materials in vacuum can be written as the product of the thermal conductivity of the bulk aggregated dust material λ_{Agg} and the Hertz factor of the pebbles H_{Pack} (see Gundlach & Blum 2012b, for details),

$$\lambda_{Net}(T) = H_{Pack} \lambda_{Agg}. \tag{A1}$$

The Hertz factor for the pebble packing and the internal heat conductivity of the aggregates are given by

$$H_{Pack} = \left[\frac{9\left(1 - \mu_{Agg}^2\right)}{4\,E_{Agg}} \pi\,\gamma_{Agg}(T)\,R^2 \right]^{1/3} \chi(\phi_{Pack}), \tag{A2}$$

and

$$\lambda_{Agg}(T) = \lambda_{Par}(T)\,H_{Agg}, \tag{A3}$$

respectively. The Hertz factor of the dust grains inside the pebbles is

$$H_{Agg} = \left[\frac{9\left(1 - \mu_{Par}^2\right)}{4\,E_{Par}} \pi\,\gamma_{Par}\,r^2 \right]^{1/3} \chi(\phi_{Agg}). \tag{A4}$$

The subscript 'Pack' denotes all parameters related to the packing of the pebbles with radii R, whereas the subscript 'Agg' indicates all parameters related to the internal structure of the pebbles, which consist of dust grains with radii r. The subscript 'Par' relates to the material properties. The symbols in equations (A1)–(A4) are defined as follows: μ is the Poisson ratio, E is the Young's modulus,

γ is the surface energy, ϕ is the volume filling factor, and $\chi(\phi)\,r = f_1 \cdot \exp(f_2\,\phi)$ is an empirical parameter that takes the packing geometry into account. The thermal conductivity of the dust material is defined as,

$$\lambda_{Par} = f_{Dust}\lambda_{Par,\,Dust} + f_{H_2O}\lambda_{Par,\,H_2O} + f_{CO_2}\lambda_{Par,\,CO_2}, \tag{A5}$$

with f_{Dust}, f_{H_2O}, and f_{CO_2} being the mass fractions of dust, H_2O ice, and CO_2 ice, respectively, and the normalization $f_{Dust} + f_{H_2O} + f_{CO_2} = 1$. Here, $\lambda_{Par,Dust}$, $\lambda_{Par,\,H_2O}$, and $\lambda_{Par,\,CO_2}$ are the thermal material conductivities of the dust and the ice components, which are summarized in Table 2. As we use the dust-to-ice mass ratio and the relative CO_2 abundance throughout this paper, we here define these relations by $f_{Dust}/f_{Ice} = f_{Dust}/(f_{H_2O} + f_{CO_2})$ and f_{CO_2}/f_{H_2O}, respectively.

In the case of no pebbles, i.e. a homogeneous dust packing, the above equations remain the same, but use $H_{Pack} = 1$.

The specific surface energy of the particles, γ_{Par}, is simply a material constant, whereas the specific surface energy of aggregated material can be written as

$$\gamma_{agg} = \phi_{agg}\,\gamma_{Par}^{5/3} \left[\frac{9\,\pi\,\left(1 - \mu_{agg}^2\right)}{r\,E_{par}} \right]^{2/3}. \tag{A6}$$

For a detailed review of these parameters, the reader is referred to Gundlach & Blum (2012b).

It is important to note that the network thermal conduction has only a weak temperature dependence (see Table A1) and decreases with increasing pebble radius as $\lambda_{Net} \propto R^{-2/3}$ (see equations A1 and A2).

Because of the high porosity, radiation can effectively transport heat through the void space between the pebbles. To simulate this radiation process, we used the photon-gas approach by Merrill (1969) and assumed that the mean free path of the photons l scales with the radius of the pebbles R. Radiative heat transport is only considered between the pebbles and is neglected inside the pebbles because of the short mean free path. The thermal conductivity due to radiation then reads

$$\lambda_{Rad}(T) = \frac{16}{3}\,\sigma\,T^3\,l(\phi_{Pack}), \tag{A7}$$

with σ being the Stefan–Boltzmann constant, and the mean free path of the photons inside the voids given by $l = e\,R\,(1 - \phi)/\phi$. The scaling parameter e was empirically determined (see Fig. 12 and equation 13 in Gundlach & Blum 2012b). Thus, the radiative heat transport linearly depends on the pebble radius and is a strong function of the temperature ($\lambda_{rad} \propto T^3$).

The transport of latent heat by sublimation and deposition is calculated by the second block (see Appendix A2)

A1.2 Efficiency function, $\eta(x)$

In this Section, the efficiency function for the outgassing through dust layers is derived. This function was originally introduced by Gundlach et al. (2011) to describe the measured decrease of the outgassing rate of an ice surface covered by a dust layer. The efficiency function reads,

$$\eta(x) = \left(1 + \frac{x}{b}\right)^{-1}. \tag{A8}$$

Here, x is the depth under the surface where the volatiles are generated and b is a scaling parameter describing the thickness of the dust layer that is required to reduce the outgassing rate into space to 50 per cent.

Table A1. Summary of the used parameters for the thermophysical model.

Parameter	Symbol	Value	Reference
Orbital			
Perihelion distance	d_p	1.24 AU	–
Sun's position*	ϑ	38°	Sierks et al. (2015)
Structural			
Radius of dust particle	r	1 μm	–
Bulk density of the comet nucleus	ρ	532 kg m^{-3}	Jorda et al. (2016)
Volume filling factor of pebble packing	ϕ_{pack}	0.6	Blum et al. (2014)
Volume filling factor inside pebbles	ϕ_{agg}	0.4	Weidling et al. (2009)
Packing structure coefficient	f_1	5.18×10^{-2}	Gundlach & Blum (2012b)
	f_2	5.26	Gundlach & Blum (2012b)
Mean free path coefficient	e	1.34	Gundlach & Blum (2012b)
Mechanical			
Poisson's ratio (particles)	μ_{par}	0.17	Chan & Tien (1973)
Poisson's ratio (pebbles)	μ_{agg}	0.17	Weidling, Guettler & Blum (2012)
Young's modulus (particles)	E_{par}	5.5×10^{10} Pa	Chan & Tien (1973)
Young's modulus (pebbles)	E_{agg}	8.1×10^{3} Pa	Weidling et al. (2012)
Specific surface energy (particles)	γ_{par}	0.1 J m^{-2}	Heim et al. (1999)
Specific surface energy (pebbles)	γ_{agg}	see equation (A6)	Gundlach & Blum (2012b)
Thermal			
Albedo	A	0.055	Sierks et al. (2015)
Heat conductivity (dust)	$\lambda_{Par, dust}$	0.5 W m^{-1} K^{-1}	Blum et al. (2017)
Heat conductivity (H$_2$O ice)	λ_{Par, H_2O}	651 W m^{-1} / T	Petrenko & Whitworth (1988)
Heat conductivity (CO$_2$ ice)	λ_{Par, CO_2}	0.02 W m^{-1} K^{-1}	www.nist.gov
Core temperature of Nucleus	T_{core}	50 K	–
Heat capacity (dust)	c_{dust}	$c_{dust} = 3.00$ kJ kg^{-1} K^{-2}	–
Heat capacity (H$_2$O ice)	c_{H_2O}	$c_{H_2O} = 0.03$ kJ kg^{-1} K^{-2}	www.nist.gov
Heat capacity (CO$_2$ ice)	c_{CO_2}	$c_{CO_2} = 0.85$ kJ kg^{-1} K^{-2}	www.nist.gov
Emissivity	ϵ	1	–
Latent heat (H$_2$O)	Λ_{H_2O}	2.86×10^{6} J kg^{-1}	Orosei et al. (1995)
Latent heat (CO$_2$)	Λ_{CO_2}	0.57×10^{6} J kg^{-1}	Mavko, Meukerji & Dvorkin (2009)
Sublimation pressure coefficients	a_{H_2O}	3.23×10^{12} Pa	Gundlach et al. (2011)
(H$_2$O)	b_{H_2O}	6134.6 K	Gundlach et al. (2011)
Sublimation pressure coefficients	a_{CO_2}	2.89×10^{12} Pa	Bryson, Cazcarra & Levenson (1974)
(CO$_2$)	b_{CO_2}	3271.1 K	Bryson et al. (1974)

Note. *: angle between surface normal and direction to Sun.

For the derivation of the efficiency function, we assume that the system reaches steady-state conditions sufficiently fast so that we can use equilibrium equations. The steady-state continuity equation reads

$$\frac{dj(x')}{dx'} = 0, \tag{A9}$$

with $j(x') = $ const being the gas mass flux (in units of kg m^{-2} s^{-1}) through the inactive layers above the respective evaporating ice, denoted by x'. With the diffusion equation

$$j(x') = -D\frac{d\rho(x')}{dx'} = \text{const}, \tag{A10}$$

we get for the gas density $\rho(x') = \rho_0 x'/x$. Here, D is the diffusion constant and x is the total thickness of the dust layer, i.e. the actual position for which the calculation is performed. This solution for the gas density fulfills the boundary conditions $\rho(x_0) = 0$ for the surface, $x_0 = 0$, of the cometary nucleus and $\rho(x) = \rho_0$ for the bottom of the inactive zone with thickness x. Hence, the gas density drops linearly with increasing height. Introducing the scaling equation for

the diffusion constant, i.e.

$$D = l_D \cdot v_D, \tag{A11}$$

with l_d and $v_D = \sqrt{\frac{8k_B T}{\pi m}}$ being a diffusion scale length and the characteristic thermal molecular velocity, we can write for equation (A10)

$$j(x, T) = -\frac{\rho_0 v_D}{x/l_D}. \tag{A12}$$

Here k_B, T, and m are the Boltzmann constant, the local temperature, and the mass of the gas molecule, respectively. In steady state, the outgassing rate equals the effective evaporation rate of the volatile and is given by the Hertz–Knudsen equation

$$j(x, T) = -(p_{Sub}(x, T) - p_{Gas}(x, T)) \sqrt{\frac{m}{2\pi k_B T}} \tag{A13}$$

$$= -(p_{Sub}(x, T) - p_0) \frac{1}{v_E}, \tag{A14}$$

with $v_E = \sqrt{\frac{2\pi k_B T}{m}}$ being the characteristic molecular velocity at evaporation. Here, $p_{Sub}(x, T)$ and $p_{Gas}(x, T) = p_0$ are the sublimation pressure, which is only a function of the local temperature T, and

the gas pressure at the base of the inactive layer, respectively. The latter is related to the gas density by the ideal gas equation

$$p_0(T) = \rho_0 \frac{k_B T}{m}. \tag{A15}$$

Equating the absolute values of equations (A12) and (A13), we get a relation for the base pressure

$$p_0(x, T) = p_{\text{Sub}}(x, T) \frac{x/l_D}{x/l_D + m\, v_d v_e/(k_B T)} \tag{A16}$$

$$= p_{\text{Sub}}(x, T) \frac{x/l_D}{x/l_D + 4}, \tag{A17}$$

re-substituting v_D and v_E as defined above. For large thicknesses of the desiccated dust layer, $L \gg l_D$, the base pressure is $p_0 \longrightarrow p_{\text{sub}}(x, T)$, whereas for low thicknesses, $x \ll l_D$, $p_0 \longrightarrow 0$. Thus, a thick dust layer favours a high gas pressure at the ice–dust interface.

The outgassing rate into space, $j_{\text{Leave}}(x, T)$, decreases with increasing dust layer thickness, because equation (A12) yields

$$j_{\text{Leave}}(x, T) = -\frac{\rho_0\, v_D}{L/l_D} \tag{A18}$$

$$= -\frac{p_0\, m\, v_D/(k_B T)}{x/l_D} \tag{A19}$$

$$= -p_{\text{sub}}(x, T) \frac{m}{k_B T} v_D \frac{1}{\frac{x}{l_D} + 4} \tag{A20}$$

$$= -p_{\text{sub}}(x, T) \frac{1}{v_E} \frac{1}{\frac{x}{4 l_D} + 1} \tag{A21}$$

$$= -p_{\text{sub}}(x, T) \frac{1}{v_E} \eta(x). \tag{A22}$$

This is the same functional form of the outgassing rate for constant temperature as a function of thickness of desiccated dust as in Gundlach et al. (2011, their equation 19 and fig. 8). Hence, $b = 4\, l_D$, is a direct measure for the diffusion scale length.

A1.3 Heat transfer equation, latent-heat cooling, and change of temperature, $T'(x, T'')$

The temperature change of the numerical layers is calculated by solving the heat transfer equation for each layer individually,

$$\rho\, c\, \frac{dT(x)}{dt} = \frac{d}{dx}\left[\lambda(T) \frac{dT(x)}{dx} \right] - Q(x, T). \tag{A23}$$

Here, ρ is the density of the material and c is the heat capacity of the material, $T(x)$ is the temperature, x is the depth, $Q(x, T)$ is an additional term which takes energy gain, or loss due to the sublimation/deposition process into account (see Davidsson & Skorov 2002, for details).

The density of the layers is always set to $\rho = 532\ \text{kg m}^{-3}$ at the beginning of the simulation runs. However, the density can locally decrease when the icy constituents sublimate or increase when ices condense. For simplicity we assume that this density change has no effect on the volume filling factor of the material. The heat capacity is derived for each time-step and numerical layer, depending on the amount of H_2O ice and CO_2 ice present in the respective layer,

$$c = f_{\text{Dust}}\, c_{\text{Dust}} + f_{H_2O}\, c_{H_2O} + f_{CO_2}\, c_{CO_2}, \tag{A24}$$

where c_{Dust}, c_{H_2O}, and c_{CO_2} are the heat capacities of the three materials used in this study (see Table A1 for details).

The source/sink term $Q(x, T)$ takes the energy loss due to sublimation and deposition at the considered location into account and reads

$$Q(x, T) = \alpha\, j(x, T)\, \Lambda(T). \tag{A25}$$
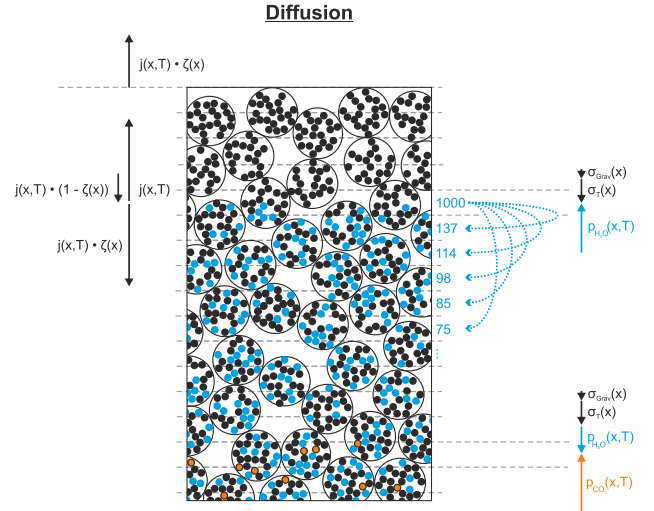

Figure A1. Sketch of the gas diffusion block. The molecules from the active layer can either escape into space, are scattered back towards the active layer, or diffuse into the interior. The inward gas transport is based on the efficiency function.

Here, $\alpha = 3\, \phi_{\text{pack}} / R$ is the surface-to-volume ratio of the material, $j(x, T)$ (see Appendix A1.2 and equation A22) is the sublimation/condensation rate of the two volatile components and $\Lambda(T)$ is the latent heat of sublimation. In case of complete ice desiccation in a layer, the source term becomes zero and the cooling switches off.

A2 2nd block: molecule redistribution and latent heat transport

This block calculates the redistribution of molecules and the corresponding transport of latent heat. For the outward migration of molecules, the rate, $j_{\text{Leave}}(x, T)$, was described in the previous subsection. Due to the assumed constant insolation at the comet's south pole around perihelion, we assume that no condensation of volatiles takes place in upper, i.e. warmer layers (see Fig. 7). For the inward-diffusing molecules, we assume that their number equals that of the outward-diffusing ones, i.e. $j_{\text{Inward}}(x, T) = j_{\text{Leave}}(x, T)$. This is clearly a crude assumptions and requires thorough consideration in future work. Latent heat is removed according to equation (A25) through the inward- and outward-diffusing molecules. For the redistribution of this heat into the interior by means of the inward-diffusing molecules, we assume that this process also follows the efficiency function shown in equation (A8). Hence, most of the molecules are deposited in the first layer, but also deeper layers can receive molecules (see Fig. A1). We chose to redistribute all the molecules into the next 15 layers beneath the active layer, denoted by x^* in Fig. 3, which is justified by the decreasing temperature with increasing depth (see Fig. 7). Based on the molecule-deposition rate, the heat gain of each layer beneath the active layer is derived (see equation A25). Backward diffusion typically leads to a much shallower temperature decrease with increasing depth than without this process.

A3 3rd block: pressure build-up and dust release

The gas pressure that acts against the tensile strength of the dust is given by p_0 in equation (A16). Using also equations (A14) and

(A22) provides us with an expression for the local gas pressure inside the considered layers, i.e.

$$p_0(x, T) = p_{Sub}(x, T)(1 - \eta(x)). \tag{A26}$$

This pressure is compared to the sum of the tensile strength, the partial pressure of the other volatile component, and the gravitational pressure of the overlying layers. When the following condition applies at any depth x

$$p_{0,H_2O}(x, T) > \sigma_T(x) + p_{Grav}(x) \tag{A27}$$

$$p_{0,CO_2}(x, T) > \sigma_T(x) + p_{Grav}(x), \tag{A28}$$

the overlying layers are ejected. Here, $\sigma_T(x)$ is the (local) tensile strength of the material, $p_{H_2O}(x, T)$ is the local partial pressure of the H_2O gas, and $p_{CO_2}(x, T)$ is the local partial pressure of the CO_2 gas. Because of the very low gravitational acceleration on the surface of **comet 67P**, the gravitational pressure of the overlying layers $p_{Grav}(x)$ was always one to three orders of magnitude lower than the gas pressure that led to the ejection event.

Since the tensile strength is a measure for the maximum stress a material can sustain until it breaks, it is important to note that the applied absolute gas pressure (and not the pressure gradient) determines whether or not an ejection event occurs. For this, we assume that the gas pressure at the surface of the comet nucleus is zero.

A4 Numerical stability

In order to test the numerical stability of the code, we performed test runs with four different values of the time resolution, $dt = 10$ s, $dt = 50$ s, $dt = 100$ s, and $dt = 200$ s, respectively. For these runs, the spatial resolution was set to $dx = 5$ mm. Then, the temperature profiles were extracted at $t = 100\,000$ s after the start of the simulation. For a better comparability, dust ejection was switched off. The dust-to-ice ratio was set to 20 and the CO_2 abundance was set to 0.15. Fig. A2 shows the resulting temperature profiles for the four different runs. Values, $dt > 200$ s, led to too large temperature gradients and, hence, to numerical instability. We decided to use $dt = 100$s, which provides numerical stability, reasonable accuracy, and relatively fast runs.

A5 Boundary conditions

We assume that the entire solar energy not scattered back into space is absorbed in the first numerical layer. The upper boundary condition is given by the energy balance equation. The surface is heated by the Sun and absorbs energy in dependence of the material's albedo A. Also, thermal re-radiation according to the Stefan–Boltzmann law is taken into account. Hence, the upper boundary condition reads

$$I_\odot \left(\frac{d_E}{d_P}\right)^2 (1 - A)\cos(\vartheta) = \epsilon\,\sigma\,T^4(x_S) - \lambda_S T(x_S)\frac{\partial T(x)}{\partial x}\bigg|_{x_S}, \tag{A29}$$

with $I_\odot$, d_E, d_P, ϑ, and $T(x_S)$ being the solar constant, the mean distance of the Earth to the Sun, the perihelion distance of comet 67P, the Sun's position with respect to the surface normal at the south pole during perihelion and the temperature of the first numerical (i.e. surface) layer, respectively.
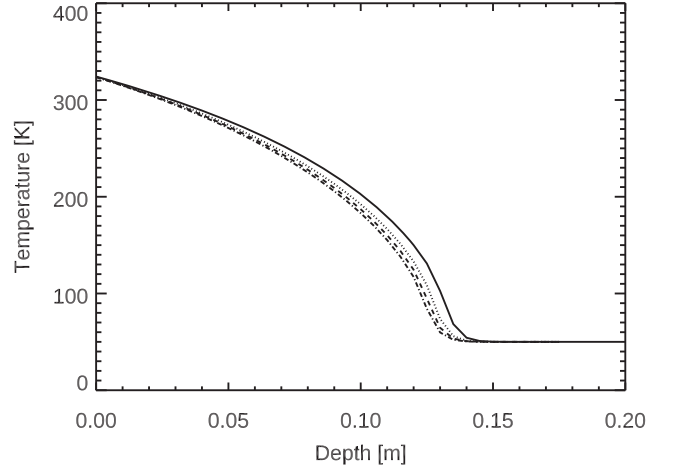

Figure A2. Resulting temperature profiles when using different time resolutions, $dt = 10$ s (dash-dotted curve), $dt = 50$ s (dashed curve), $dt = 100$ s (dotted curve), and $dt = 200$ s (solid curve). Values, $dt > 200$ s, are numerically unstable. These runs were performed for a dust-to-ice ratio of 20 and a CO_2–ice content of 0.15. Ejection of layers was switched off for a better comparability.

The lower boundary condition requires that no temperature change occurs in the last layer, i.e.

$$\frac{dT(x)}{dt}\bigg|_{x_B} = 0. \tag{A30}$$

Here, x_B denotes the position of the last layer (measured from the top). The code aborts the simulation if a temperature of 50.1 K is detected in the last layer.

APPENDIX B: DEFINITION OF THE OUTPUT PARAMETERS

The model provides different output parameters, namely the outgassing rates of the two volatile components, $\dot{\gamma}_{H_2O}$ and $\dot{\gamma}_{CO_2}$ (in units of kg m^{-2}, extrapolated to a total surface of 10^7 m^2), the total dust ejection rate, $\dot{\delta}_{Dust}$ (also in units of kg m^{-2}, extrapolated to a total surface of 10^7 m^2), the mean size of the emitted dust chunks, x_{H_2O} and x_{CO_2} (depending on the release by H_2O or H_2O vapour), and the H_2O–ice content, f_{H_2O}(Chunk), of the ejected chunks. In the following, we present how the different model output parameters are defined.

B1 Outgassing rates, $\dot{\gamma}_{H_2O}$ and $\dot{\gamma}_{CO_2}$

The outgassing rates of the H_2O and the CO_2 gas into space are directly derived from equation (A22). Then, the values are multiplied by $S = 10^7$ m^2 to obtain the entire outgassing rate of the Southern hemisphere of the comet nucleus.

$$\dot{\gamma}_{H_2O,CO_2} = \frac{S}{t_{Sim}} \sum_{t=0}^{t_{Sim}} \sum_{x=0}^{x_{In}} j_{Leave}(x, T)\Delta t. \tag{B1}$$

Here, the t_{Sim} is the total simulation time (the simulation stopped when 50 ejection events were recorded). x_{In} denotes the last numerical layer and Δt is the time-step of the simulation.

B2 Dust ejection rate, $\dot{\delta}_{Dust}$

The total dust ejection rate is a measure of the total mass of solid material lost into space per second. This includes the mass ejected by H_2O- and by CO_2-driven activity as well as the solid H_2O ice in the large chunks (the latter entirely ejected by CO_2-driven activity). The mass-loss rate is derived by summation of the erosion depths over all ejection events,

$$\dot{\delta}_{Dust} = \frac{S}{t_{Sim}} \left(\sum_{i_{H_2O}=1}^{N_{H_2O}} x_{i_{H_2O}} \rho_{Chunk,H_2O} + \sum_{j_{CO_2}=1}^{N_{CO_2}} x_{j_{CO_2}} \rho_{Chunk,CO_2} \right).$$
(B2)

Here, i_{H_2O} and j_{CO_2} are the indices of the dust-ejection events (counted for each ice species individually) and N_{H_2O} and N_{CO_2} are the total numbers of the erosion events driven by water ice or carbon-dioxide ice, respectively. The simulations are stopped after $N_{H_2O} + N_{CO_2} = 50$ ejection events have occurred. As before, $S = 10^7 \, m^2$ is the total active area, $\rho_{Chunk,H_2O} \approx 532 \, kg \, m^{-3}$, and $\rho_{Chunk,CO_2} \approx 532 \, kg \, m^{-3}$ are the mass densities of the ejected chunks and t_{Sim} is the total simulation time.

B3 Ice content of the chunks, ξ_{H_2O}

Because the CO_2 sublimation front retreats faster than the H_2O sublimation front, the activity of CO_2 can eject H_2O–ice containing chunks. Since the code tracks the number of ice molecules in each layer, the mean ice content can be derived through

$$\xi_{H_2O} \sum_{x=0}^{x_{CO_2}} \frac{f_{H_2O}(x)}{f_{H_2O,Ini}}.$$
(B3)

Here, x_{CO_2} is the depth at which the ejection criterion is fulfilled for the CO_2 gas (see equation A27). Furthermore, $f_{H_2O}(x)$ and $f_{H_2O,Ini}$ are the actual water ice content at position x and the initial water ice content, respectively. Chunks ejected by the activity of H_2O cannot contain H_2O or CO_2 ice.

B4 Size of the ejected chunks, x_{H_2O} and x_{CO_2}

The mean size of the ejected chunks, x_{H_2O} and x_{CO_2}, is derived by calculating the arithmetic mean of all ejection depths $x_{H_2O,i}$ and $x_{CO_2,i}$

$$x_{H_2O} = \frac{1}{N_{H_2O}} \sum_{i=1}^{N_{H_2O}} x_{H_2O,i}$$
(B4)

$$x_{CO_2} = \frac{1}{N_{CO_2}} \sum_{i=1}^{N_{CO_2}} x_{CO_2,i},$$
(B5)

and $N_{H_2O} + N_{CO_2} = 50$. The CO_2-driven activity generally ejects larger chunks than the H_2O-driven activity.

B5 Slope parameter

In our thermophysical model, H_2O activity drives the ejection of small chunks, whereas the activity of CO_2 ejects larger chunks. Hence, we defined the slope parameter $Q_{Slope\,Ratio}$ to compare the ejected mass ratios (large versus small chunks) provided by the simulation runs with the *Rosetta* observations (mass-loss distribtion provided by Ott et al. 2017). The slope parameter is defined as

$$Q_{Slope\,Ratio} = \frac{\Pi_{Simulation}}{\Pi_{Rosetta}},$$
(B6)

with $\Pi_{Simulation}$ defined by

$$\Pi_{Simulation} = \frac{\log[(x_{CO_2} N_{CO_2})/(x_{H_2O} N_{H_2O})]}{\log[x_{CO_2}^3/x_{H_2O}^3]},$$
(B7)

assuming that the ejected chunks are cubic in shape.

We estimated the slope of the *Rosetta* dust–size distribution using the data published by Ott et al. (2017, their fig. 10 and table 4) to be

$$\Pi_{Rosetta} = +1/2 \qquad \text{for} \qquad x_{CO_2} \leq 12.3 \, cm \quad \text{(B8)}$$

$$= -1/2 \qquad \text{for} \qquad x_{CO_2} > 12.3 \, cm. \quad \text{(B9)}$$

APPENDIX C: ROLE OF BACK DIFFUSION: COMPARISON OF RUNS WITH AND WITHOUT BACK DIFFUSION

Table C1 presents the A3 runs with (black numbers) and without back diffusion (italic numbers). As can be seen by comparing the numbers, the difference between the runs is less than 15 per cent.

Table C1. Summary of all A3 cases with back diffusion enabled (black numbers) and with back diffusion disabled (italic numbers).

Variable tensile strength										
Input parameters				Output parameters						
Scale length	Radius	D:I	CO_2 Cont.	$\dot{\gamma}_{H_2O}$ / $\dot{\gamma}_{H_2O,R}$	$\dot{\gamma}_{CO_2}$ / $\dot{\gamma}_{CO_2,R}$	$\dot{\delta}_{Dust}$ / $\dot{\delta}_{Dust,R}$	$Q_{Slope\ ratio}$	Size (x_{CO_2})	Ice Cont.	$\bar{\sigma}(x_{CO_2})^{\dagger}$
1 cm	5 mm	2	0.16	2.22	4.36	2.89	0.74	11.3 cm	0.87	0.3 Pa
1 cm	*5 mm*	*2*	*0.16*	*2.20*	*4.45*	*2.95*	*0.71*	*12.9 cm*	*0.87*	*0.3 Pa*
2 cm	5 mm	2	0.15	1.96	2.77	1.89	0.85	6.4 cm	0.83	0.5 Pa
2 cm	*5 mm*	*2*	*0.15*	*2.05*	*3.34*	*2.37*	*0.83*	*6.2 cm*	*0.85*	*0.5 Pa*
2 cm	5 mm	2	0.16	2.05	3.60	2.39	0.84	15.2 cm	0.85	0.3 Pa
2 cm	*5 mm*	*2*	*0.16*	*2.06*	*3.68*	*2.44*	*0.83*	*14.4 cm*	*0.84*	*0.3 Pa*
3 cm	5 mm	10	0.21	1.35	0.91	1.77	1.60	14.4 cm	0.48	0.4 Pa
3 cm	*5 mm*	*10*	*0.21*	*1.39*	*0.91*	*1.79*	*1.58*	*13.7 cm*	*0.49*	*0.4 Pa*
4 cm	5 mm	3	0.23	2.22	4.16	2.50	0.90	8.4 cm	0.79	0.6 Pa
4 cm	*5 mm*	*3*	*0.23*	*2.26*	*4.14*	*2.52*	*0.87*	*6.7 cm*	*0.83*	*0.6 Pa*
4 cm	5 mm	7	0.21	1.75	1.44	2.00	1.35	7.9 cm	0.58	0.6 Pa
4 cm	*5 mm*	*7*	*0.21*	*2.00*	*1.53*	*2.13*	*1.23*	*6.0 cm*	*0.63*	*0.6 Pa*
4 cm	5 mm	7	0.22	1.79	1.61	2.10	1.28	8.4 cm	0.60	0.6 Pa
4 cm	*5 mm*	*7*	*0.22*	*1.86*	*1.62*	*2.13*	*1.27*	*8.8 cm*	*0.60*	*0.6 Pa*
4 cm	5 mm	7	0.23	1.85	1.77	2.24	1.21	9.0 cm	0.61	0.6 Pa
4 cm	*5 mm*	*7*	*0.23*	*1.92*	*1.76*	*2.23*	*1.20*	*8.2 cm*	*0.62*	*0.6 Pa*
5 cm	5 mm	6	0.24	1.77	2.00	2.07	∞	15.9 cm	0.61	0.5 Pa
5 cm	*5 mm*	*6*	*0.24*	*1.77*	*1.79*	*2.04*	*∞*	*15.6 cm*	*0.61*	*0.5 Pa*

Fixed tensile strength									
Input parameters				Output parameters					
Tensile Str.	Radius	D:I	CO_2 Cont.	$\dot{\gamma}_{H_2O}$ / $\dot{\gamma}_{H_2O,R}$	$\dot{\gamma}_{CO_2}$ / $\dot{\gamma}_{CO_2,R}$	$\dot{\delta}_{Dust}$ / $\dot{\delta}_{Dust,R}$	$Q_{Slope\ Ratio}$	Size (x_{CO_2})	Ice Cont.
0.4 Pa	12.5 mm	4	0.15	2.41	3.58	4.64	1.22	7.2 cm	0.59	–
0.4 Pa	*12.5 mm*	*4*	*0.15*	*2.14*	*3.52*	*4.26*	*0.96*	*11.3 cm*	*0.60*	*–*
0.5 Pa	12.5 mm	2	0.15	2.34	4.57	3.29	1.09	14.1 cm	0.56	–
0.5 Pa	*12.5 mm*	*2*	*0.15*	*2.57*	*4.15*	*2.80*	*1.11*	*13.5 cm*	*0.55*	*–*
0.4 Pa	10 mm	2	0.15	2.30	4.31	3.24	0.70	10.1 cm	0.47	–
0.4 Pa	*10 mm*	*2*	*0.15*	*2.18*	*3.73*	*2.65*	*0.79*	*8.6 cm*	*0.50*	*–*
0.7 Pa	12.5 mm	4	0.30	3.51	6.39	3.79	0.70	20.0 cm	0.58	–
0.7 Pa	*12.5 mm*	*4*	*0.30*	*3.61*	*6.34*	*3.60*	*0.69*	*19.5 cm*	*0.53*	*–*

Notes. Radius: radius of the dust aggregates; D:I: dust-to-ice ratio; R: Rosetta; Size: mean size of the large chunks; ∞: only CO_2-driven ejection events.
$\dagger$: $\bar{\sigma}(x_{CO_2})$ is the mean tensile strength at location of breakup.
*: the infinite value is ignored.

This paper has been typeset from a TEX/LATEX file prepared by the author.